Materials Horizons

ROYAL SOCIETY OF CHEMISTRY

MINIREVIEW

View Article Online
View Journal | View Issue

Cite this: *Mater. Horiz.*, 2023, **10**, 1234

Noble metal nanodendrites: growth mechanisms, synthesis strategies and applications

Ke Guo, Dongdong Xu, * Lin Xu,* Yafei Li and Yawen Tang

Inorganic nanodendrites (NDs) have become a kind of advanced nanomaterials with broad application prospects because of their unique branched architecture. The structural characteristics of nanodendrites include highly branched morphology, abundant tips/edges and high-index crystal planes, and a high atomic utilization rate, which give them great potential for usage in the fields of electrocatalysis, sensing, and therapeutics. Therefore, the rational design and controlled synthesis of inorganic (especially noble metals) nanodendrites have attracted widespread attention nowadays. The development of synthesis strategies and characterization methodology provides unprecedented opportunities for the preparation of abundant nanodendrites with interesting crystallographic structures, morphologies, and application performances. In this review, we systematically summarize the formation mechanisms of noble metal nanodendrites reported in recent years, with a special focus on surfactant-mediated mechanisms. Some typical examples obtained by innovative synthetic methods are then highlighted and recent advances in the application of noble metal nanodendrites are carefully discussed. Finally, we conclude and present the prospects for the future development of nanodendrites. This review helps to deeply understand the synthesis and application of noble metal nanodendrites and may provide some inspiration to develop novel functional nanomaterials (especially electrocatalysts) with enhanced performance.

Received 14th November 2022,
Accepted 5th January 2023

DOI: 10.1039/d2mh01408d

rsc.li/materials-horizons

1. Introduction

It is easy to find abundant colorful superstructures in nature like flowers, plants, snowflakes, and trees that exhibit self-assembled hierarchy and repetition. Inspired by nature, scientists always tried to mimic these interesting superstructures especially in the fields of chemistry and materials. For instance,

Jiangsu Key Laboratory of New Power Batteries, Jiangsu Collaborative Innovation Center of Biomedical Functional Materials, School of Chemistry and Materials Science, Nanjing Normal University, Nanjing, Jiangsu 210023, China. E-mail: ddxu@njnu.edu.cn, xulin001@njnu.edu.cn

Ke Guo

Ke Guo received her master's degree from Nanjing Normal University in 2020. She is currently pursuing her PhD in the School of Chemistry and Materials Science at Nanjing Normal University. Her research interests relate to the design and synthesis of two-dimensional noble metal nanomaterials and their applications in energy storage and conversion.

Dongdong Xu

Dongdong Xu is currently an associate professor in the School of Chemistry and Materials Science at Nanjing Normal University, China. He received his BS degree in chemistry from Nankai University in 2009, and PhD from Shanghai Jiao Tong University in 2014, under the supervision of Prof. Shunai Che. His research interests mainly focus on the construction of inorganic metallic architecture based on the self-assembly of designed surfactants, and electrocatalytic applications.

semiconductor materials are easily produced as branched structures due to the presence of two or more crystal structures, *i.e.*, polymorphism, which often produces two composite crystal structures in one nanomaterial. Related topics have been extensively studied.[1–3] Taking the CdSe tetrapod as an example, the zinc blende structure of CdSe is favored in the nucleation stage. As the crystal grows with decreasing monomer concentration, the edge of the zinc blende core turns to form a hexagonal wurtzite structure.[4] This non-equilibrium growth process results in a dendritic structure of four rods with tetrahedral angles. It was also discovered that dendrites occur in semiconductors with symmetric cubic lattices due to the changes in growth patterns *via* dipole–dipole interactions, resulting in chainlike aggregates.[5] Not surprisingly, such dendritic growth is also presented in other inorganic systems like noble metal nanomaterials.[6] The growth process of nanodendrites is emphasized to be fast and monomers need to be selectively deposited at the tip sites to obtain nanodendrite structures. The noble metals (mainly platinum (Pt), palladium (Pd) and gold (Au)) allow fast growth processes due to their high reduction potential ($PdCl_4^{2-}/Pd^0$ = 0.62 V, $PtCl_4^{2-}/Pt^0$ = 0.73 V, and Au^{3+}/Au^0 = 1.498 V). In contrast, non-noble metals, copper (Cu) for example, have a relatively low reducing electrode potential (Cu^{2+}/Cu^0 = 0.337 V), making their growth rate inherently slower than that of noble metals, so it is difficult for non-noble metals to obtain well-defined nanodendrites compared to noble metals.

Relatively few reserves of noble metals on the earth inevitably lead to expensive cost. Affordability for both basic experiments and practical applications must be prudently considered and the cost reductions for the usage of noble metals are thus necessary. There is abundant evidence that the higher the atom utilization, the higher the catalytic performance exhibited in the field of electrocatalysis.[7,8] For instance, the efficient utilization of Pt atoms can improve their activity and selectivity in many kinds of electrocatalytic reactions.[9–11] In order to realize high atomic efficiency, it is a good way to expose as many atoms as possible on the surface of metallic crystals, which requires the rational design of special crystallographic structure/morphology. In recent years, many efforts have been made to engineer the noble metal crystals where a large number of interesting nanostructures/morphologies have been reported, such as nanowires, nanosheets, nanoframes, nanomeshes, hollow nanospheres, and supported single atom nanostructures. These obtained nanomaterials have shown remarkable performances in various electrocatalyses.[12–19]

The physical and chemical properties of noble metal nanocrystals can be extensively tailored by adjusting their size and shape.[20] Some nanocatalysts with different morphologies (*e.g.*, cubes and octahedrons) can expose different crystal facets, which bring about different atomic arrangements on the surface and directly affect the adsorption energy of intermediates in catalytic reactions.[21–23] In addition, the ultrathin and porous structures usually boost the electron/mass transfer ability and thus the activity.[24,25] A mass of electrocatalysts have been

Lin Xu

Lin Xu received his BS in 2004 from Nantong University and his PhD in 2010 from Nanjing University under the guidance of Prof. Wenhua Hou. After the postdoctoral stage at Indiana University and Nanyang Technological University, he moved to Nanjing Normal University and is currently an associate professor in the School of Chemistry and Materials Science. His research interests mainly include the synthesis of functional nanomaterials and their energy conversion and storage.

Yafei Li

Yafei Li received his BS in 2006 in materials chemistry from Chongqing University and his PhD in 2011 in inorganic chemistry from Nankai University under the guidance of Prof. Panwen Shen and Prof. Zhen Zhou. After a postdoctoral stage at the University of Puerto Rico, Rio Piedras campus, with Prof. Zhongfang Chen, he moved to Nanjing Normal University, where he was appointed as a professor in the School of Chemistry and Materials Science in 2013. His research interests include novel low-dimensional nanomaterials and new energy nanomaterials.

Yawen Tang

Yawen Tang received his BS degree and MS degree from Nanjing Normal University in 1992 and 2002, respectively, and his PhD from Nanjing University of Science & Technology in 2011. He is currently a full professor at the College of Chemistry and Materials Science at Nanjing Normal University. His main research interests are the synthesis and assembly of nanomaterials, and their applications in batteries, fuel cells, and photocatalysis.

designed based on these principles. Actually, not only in the electrocatalysis field, they still show promising applications in common organic catalysis, sensing, imaging, electronics/photonics, and therapy. Among numerous structures and morphologies, nanodendritic architecture possesses special characteristics, such as ultrathin structures like nanosheets (only for two-dimensional (2D) nanodendrites), abundant channels like mesoporous structures, a highly open structure similar to nanoframes, *etc.* Nanodendrites exhibit unique advantages among the above nanomaterials. For example, nanodendrites have the advantages of both nanowires and nanosheets, and each branch can be regarded as a nanowire, while the whole structure can be used as a skeleton to support the individual dispersion of each branch. In addition, compared to nanoframes and hollow nanospheres, nanodendrites are synthesized in a simple way and can usually be completed in a one-step reaction without a subsequent etching process, so there is no waste of noble metal precursors in the synthesis process. Compared with nanomeshes, nanodendrites are more easily dispersed in solvents and are less agglomerated in the electrocatalytic process. Compared with single atom nanomaterials, nanodendrites do not need to find a carrier that can be stably anchored in the synthesis, so the method can be universally extended to other noble metal or non-noble metal catalysts. More importantly, single atom nanocatalysts were originally designed to reduce the noble metal loading while still achieving high catalytic activity. However, in practice, the desired activity is not always obtained, and the loading and structure are still limited. In contrast, nanodendrites, due to their highly branched nature, expose as many available atomic sites as possible, and the desired catalytic activity can usually be obtained by changing the catalyst components. Therefore, engineering of dendritic morphology has become an interesting issue especially in the field of electrocatalysis where the design of dendritic structures can not only greatly improve the electrocatalytic performance but also help to fully exploit the corresponding structure–function relationship.

As is well known, the approach for synthesizing nanocrystals generally involves three steps: reduction of metal precursors, nucleation of metal atoms, and growth of metal nuclei to well-defined shapes.[26,27] The prerequisite for the formation of nanodendrites is the selective deposition of metal atoms in some sites of the nucleus. However, the crystal structures of noble metals are highly symmetric and inherently lack the driving force for anisotropic growth. Therefore, the crystal symmetry must first be broken to induce branched or dendritic growth. That is, the formation of nanodendrites must dominate in the kinetic growth or else thermodynamically stable nanoparticles will be produced. To date, some excellent reviews have discussed the advances in the design of branched nanocrystals/nanodendrites. For example, Xia and coworkers reviewed the procedures and mechanisms of branched metal nanocrystals and briefly described their application in the field of electrocatalysis.[28] Lee and coworkers reviewed the synthetic approaches and electrochemical applications focusing on Pt-group metals (PGMs).[29] In recent years, with the continuous development of nanosynthesis chemistry, scientific research about the formation mechanism of nanodendrites (especially for organic template-mediated mechanisms) and their electrocatalytic mechanism has been increasingly explored. For example, the development of *in situ* electron microscopy allows direct observation of the growth process of noble metals, which facilitates our in-depth understanding of the growth of nanodendrites. Our group has made advancing contributions to the development of 2D nanodendrites, realizing the synthesis of highly branched noble metal nanodendrites using a surfactant-confined method. However, there is no relevant review available, and in order to expose more readers to the frontier research in the field of nanodendrite synthesis, it is greatly necessary to review this topic about the growth mechanisms, synthesis approaches of advanced noble metal-based nanodendrites, and the corresponding practical applications. Moreover, a deep discussion about the electrocatalytic mechanism of nanodendrites has a very important impact on the current research in the field of electrocatalysis.

This review shows comprehensive summaries of many nanodendrites and highlights their significance in various applications. Section 2 presents the formation mechanisms from the views of both theoretical simulations and practical diversified growth models, which will help to design a more advanced structure. Section 3 presents several typical synthesis approaches. It can be summarized from the reported works that the preparation technology of three-dimensional (3D) nanodendrites is close to maturity, while for 2D nanodendrites, there is still a lot to explore. In Section 4, we discuss the applications of noble metal nanodendrites, mainly focusing on electrocatalysis. A large number of evidence shows that nanodendrite structures exhibit high activity, stability, and selectivity. In addition, some examples of their applications in the biosensing and therapeutic field are presented, showing their broad application prospects. Finally, in Section 5, we describe perspectives and future opportunities for the in-depth development of nanodendrites.

2. Growth mechanism of noble metal nanodendrites

Thermodynamically controlled synthesis can only produce very limited shapes and surface structures because under these conditions the atoms tend to diffuse exclusively to the surface with the lowest Gibbs free energy. Nanocrystals with high anisotropy like nanodendrites require strictly kinetically controlled synthesis.[28] When the growth rate exceeds the thermodynamically controlled range, it is reflected not only in the difference between the growth rates of the high- and low-energy crystal surfaces, but also in the fact that the addition of atoms is faster than the diffusion of adsorbed atoms, preventing the deposition of atoms at low-energy sites and resulting in anisotropic overgrowth.[30]

A prerequisite for the formation of nanodendrites is the preferential growth of monomers at the tips of the dendrites

during the growth process. Experimental conditions are usually used to adjust kinetic parameters to obtain defined nanodendrites by controlling the reaction temperature, the addition sequence of reactants, the type and dropping rate of the metal precursors, the type and concentration of the surfactants or other additives, pH of solutions and solvents, supersaturation of precursor monomers, *etc*.[6,31–39] In order to reduce the surface energy, nanoparticles which are formed during the nucleation period tend to coalesce with each other, and different aggregation modes lead to different final product structures.[40] The growth process of nanodendrites can be tracked by a time-dependent experiment to determine the growth mechanism. Here, we discuss several types of growth mechanisms for nanodendrites. Two fundamental mechanisms and then several extended mechanisms are presented: seed-mediated growth, surfactant-mediated growth, chemical etching growth and other growth models, all of which have been widely used for synthesizing nanodendrites. These growth mechanisms are described in detail below, with particular emphasis on surfactant-mediated growth.

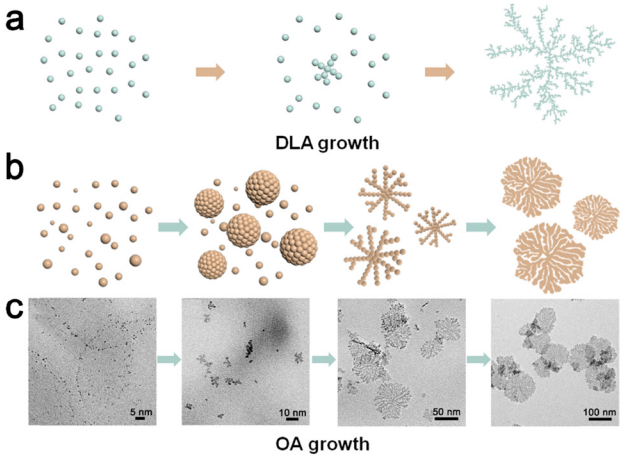

Fig. 1 Scheme illustration of two fundamental growth mechanisms: (a) DLA growth and (b) OA growth. The nanodendrites in (a) are adapted with permission from ref. 41. Copyright 1981, American Physical Society. (c) TEM images of Pt nanostructure obtained at the reaction period of 10 min, 30 min, 2 h, and 4 h. Adapted with permission from ref. 42. Copyright 2019 American Chemical Society.

2.1 Fundamental mechanism

2.1.1 Diffusion-limited aggregation (DLA) growth. In 1981, Witten and Sander proposed the diffusion-limited aggregation (DLA) model, in which they successfully simulated dendrite growth.[41] In this work, they built a square lattice in which a seed particle was placed in the middle of the lattice in the initial state, and then diffusion particles were randomly added, which moved randomly through the lattice in a manner similar to Brownian motion. If the central seed touches another particle, the two particles will stick together. If some particles exceed the fixed circumferential distance from the central seed, they will be absorbed by the newly formed seed sites at the outer boundary. As the particles continue to aggregate, a large skeleton in the shape of dendrites is found to form, and the remaining random particles in the system will preferentially adsorb at the tip of the branches, eventually forming the nanodendrites as shown in Fig. 1a. Although this mechanism has been modified and developed in later studies, its contribution to the field of nanodendrites regarding the growth mechanism is quite important.[43–50] Kern and coworkers studied diffusion-limited aggregation of silver (Ag) atoms on a Pt(111) surface using a scanning tunnelling microscope.[6] They pointed out that deposition flux affects the crossover from ramified to dendritic patterns, *i.e.*, the growth rate of aggregates. A relatively high flux favors the generation of dendritic aggregate.

In the DLA model proposed by Witten and Sander, particles adhere to selected seeds through a random walk process to form aggregates, so the resulting aggregate should be continuous. However, in actual experiments, the results were not as predicted. Kawai found that isolated nanodendrites were formed in their system, so researchers believed that the current formation process of dendritic assemblies cannot be explained by the DLA. There should be another mechanism to explain this phenomenon.[51]

2.1.2 Oriented attachment (OA) aggregation growth. OA growth was discovered in 1998 by Penn and Banfield, who stated that neighbouring particles spontaneously organize into self-organizing particles and share a common crystallographic orientation.[52] With the reduction of the precursors, the nanoparticles are first generated and gather together along the same crystallographic orientation and start branching growth with the assistance of external conditions,[53,54] as shown in Fig. 1b and c (to simplify the model, only 2D growth is shown in the figure). Accelerated autocatalytic reduction is another name that is also commonly used by researchers.[55–57] *In situ* electron microscopy was used to observe the growth mechanism of nanomaterials in real time.[58] It was found that dislocations are usually unavoidable when nanocrystals grow through the OA mechanism. When the mismatch between the two particles is small, the atoms will be reoriented by diffusion to eliminate the interface defects, thus maintaining single crystal characteristics.[59–61] For example, Zheng and coworkers employed *in situ* electron microscopy to track the growth process of Pt_3Fe nanorods in real time. It was observed that the entanglement of polycrystalline nanoparticle chains was formed by the attachment of shape-oriented nanoparticles, which are then straightened and corrected to form single crystal nanorods. This work has important implications for our understanding of the self-assembled growth pattern of nanodendrites.[62] Gu and coworkers reported the preparation of PtRu nanodendrites by an OA growth mechanism.[63] The reduction of Pt precursors with the assistance of hydrogen (H_2) as a reducing agent guided the subsequent directed growth to finally obtain single-crystalline PtRu nanodendrites. During this process, H_2 can partially cap the hydrogen-active surface and thus inhibit growth along this surface and promote the growth along the branch tips.[64] Yang and coworkers used Zn microparticles as a reducing agent to synthesize the first

surfactant-free Ag nanodendrites.[65] Ag was grown along ⟨100⟩, ⟨111⟩ and ⟨100⟩ directions in successive generations from stem/branch to subbranches to generate the final nanodendrites.

The misoriented attachment mechanisms also facilitate the formation of highly anisotropic nanostructures but result in the polycrystalline structure and the presence of defects at the interface.[66] Mirsaidov and coworkers carefully investigated the reasons for the occurrence of such misoriented attachment mechanisms in nanoparticles. The results showed that whether misoriented attachment occurs can be determined by the critical angle at which the nanoparticles reorient or generate the formation of defects during the coalescence. Using 10 nm Au nanocrystals as an example, both *in situ* experiments and full-atom molecular dynamics simulations pointed out that coherent defect-free bonding occurs when two nanocrystals are aligned within a critical angle. If the critical angle is exceeded, *i.e.* 15°, defects form at the interface.[67] Therefore, there are many reports on polycrystalline nanodendrites. For instance, Zhang and coworkers reported polycrystalline PtRu nanodendrites.[68] They investigated the growth process of the PtRu nanodendrites and found the existence of crystal boundaries between two branches by comparing the growth orientation of different branches. It can be concluded that the polycrystalline nature of PtRu nanodendrites is triggered by imperfect oriented attachment at the interface. The adhesion angle of colliding nanoparticles is a key parameter affecting the formation of single and polycrystalline structures, and this collision can be changed by adjusting the reaction parameters.

2.2 Seed-mediated growth

Heterogeneous seed-mediated growth is an effective method for manipulating the branched growth, which differs in that the core and the outer noble metals respectively possess different chemical properties. It is an extension of the OA growth mechanism to a certain extent and can be used to precisely control the morphology and composition of metal nanostructures.[72] The surface properties of the seed and the degree of lattice mismatch with the second noble metal will affect the subsequent growth. Xia and co-workers proposed a seed-mediated formation mechanism to synthesize Pd–Pt bimetallic nanodendrites in 2009. In this reaction, truncated octahedral Pd NCs were used as seeds. Pt was then deposited on Pd cores, and these Pt sites acted as catalytic sites for the reduction of residual Pt precursors, thus ensuring that the reduction took place preferentially on Pt sites rather than on Pd sites.[55] This selective deposition of atoms provides an opportunity for the generation of nanodendrites. Yang and coworkers reported Au twin particles as seeds for the fabrication of noble bimetallic nanoparticles with dendritic structures. The shell metals can be extended to Pt, Pd, Ru, and Ir. They found that the crystal defects in the Au seeds are essential for the formation of dendritic Au–Pt structures.[73] This is because the energy of the grain boundary sites is higher than that of the sites on the plane facet, so the shell metals deposit preferentially at the high-energy sites, eventually generating nanodendrites along the five sites of the Au twin particles. Yang and coworkers also reported that the shapes of formed Pt multipod depended on the number and type of twin planes in seed crystals.[74] Understanding the growth mechanism of five-fold twins is helpful to improve the existing experimental protocols. For example, Li and coworkers observed the formation of five-fold twins and revealed the two types of formation mechanisms for five-fold twins with *in situ* electron microscopy.[75] This provides convenience for the preparation of nanodendrites by the seed-mediated method.

Tilley and coworkers discovered Au–Ru branched nanoparticles (NPs) with Au icosahedral as seeds.[69] In fact, there is a large lattice mismatch between Au and Ru. Au is generally stable with a face-centered cubic (fcc) structure, while Ru tends to form a hexagonal close packed (hcp) structure. Therefore, it is actually unfavorable to generate heterogeneous growth between these two crystal structures. They explored the growth mechanism of branched Au–Ru NPs as shown in Fig. 2a. In the first stage, Ru atoms are first reduced and encapsulated on Au nuclei to form amorphous shell nanoparticles, and then the remaining amorphous Ru clusters tended to coalesce and crystallize in order to reduce the surface energy. In the third growth stage, the arms form well-defined faceted branches, resulting in a hexagonal pyramid branching shape. The difference with the common OA model in this work is that the Ru of the hcp crystal structure first exists as an amorphous state on the Au surface and only gradually crystallizes into a branching structure as the reaction proceeds further, with an intervening transition state to compensate for the gap in the lattice mismatch. This work provides a reference for the preparation of dendritic structures with non-fcc shells.

Self-branch growth of noble metals can also be induced by adjusting the reaction conditions. For example, Xie and coworkers reported Rh nanobranches (NBs) and discussed their growth mechanism, and no heterogeneous seed growth was found in this work.[70] In the early stage, thermodynamically stable icosahedra nanoparticles with multiple {111} twins were formed and served as seeds for further growth. With further reduction of Rh precursors, multi-pod nanostructures were formed. As the reaction continued, the arm lengths grew longer and the number of arms increased, eventually forming a 3D dendritic structure (Fig. 2b).

There are also some reports about using nanodendrites as seeds, and this method can achieve a perfect replication of the seed structure.[76] This method includes many different processes: (1) atomic diffusion method. As proposed by Li and coworkers, branched Pt is prepared as seeds, and then another metal–Ni is diffused into the seeds to form bimetallic nanodendrites.[71] (2) Epitaxial growth method. For example, Xu and coworkers prepared Pt@Pd NDs by epitaxially growing Pd nanosheets on the edges of Pt NDs using the prepared Pt NDs as seeds.[42] (3) Galvanic displacement method. Tang and coworkers proposed that Pd^{II} can enter into the lattice of the prepared PtCu seeds to form ternary alloy nanodendrites through galvanic displacement.[80] (4) Sequential reduction method. The sequential reduction due to different reduction potentials between these noble metal precursors facilitates the

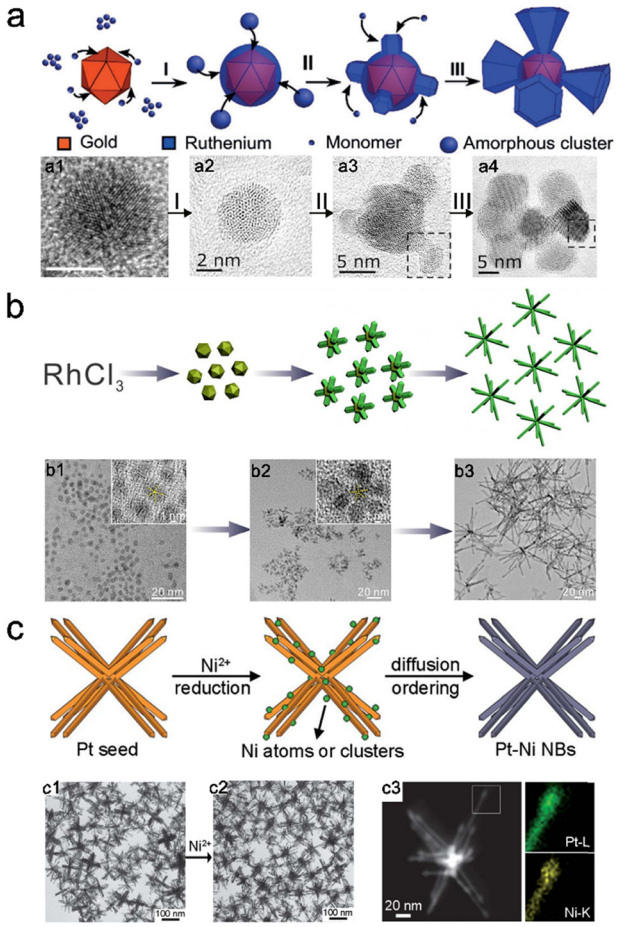

Fig. 2 (a) Growth mechanism of branched Au–Ru NPs. a1–a4: HRTEM image of Au NPs, spherical Ru NP at 8 h, 16 h, and 24 h, respectively. Adapted with permission from ref. 69. Copyright 2018 Wiley-VCH Verlag GmbH & Co. KGaA, Weinheim; (b) growth schematic of Rh NBs. b1–b3: TEM images of the Rh NB intermediates that were collected at 25 min, 30 min, and 6 h, respectively. Adapted with permission from ref. 70. Copyright 2018 American Chemical Society; (c) schematic illustration of the controlled synthesis of Pt–Ni nanobundles by a seed-based diffusion route. c1–c3: TEM image of Pt seeds, Pt–Ni nanobundles, and EDX mapping of Pt–Ni nanobundles. Adapted with permission from ref. 71. Copyright 2012 The Royal Society of Chemistry.

fabrication of core–shell nanodendrites. For instance, Liu and coworkers synthesized AuPdPt spherical nanodendrites in which Pd was preferentially reduced on Au seeds.[81] Pt was then alloyed with Pd *via* a galvanic replacement reaction and incorporated into the nanodendrite structure.

Song and coworkers described the *in situ* seeds generation method.[57,82] They proposed a ZnP-based and SnP-based photocatalytic seeding mechanism. For example, absorption of visible light by ZnP yields ZnP*, which is a strong reducing agent that rapidly reduces Pt^{2+} to Pt^{0}. This method allowed easy manipulation of the size and uniformity of platinum nanodendrites by white light.

2.3 Surfactant-mediated growth

Surfactants are a class of substances with hydrophilic heads and hydrophobic tails that enable them to self-assemble into diverse aggregates (micelles) in solution, allowing inorganic species to grow in nano-confined spaces. Most of the nanodendrites are synthesized under the presence of additional reagents, such as surfactants.[33] Because organic surfactants have a powerful stabilizing effect on some crystal facets, the ligands on the crystal surface can reduce the total surface free energy of nanodendrites. Secondly, surfactants also have the structural directing effect in order to modify their growth habit by chemical or physical adsorption, directing the growth of nanomaterials in the highly anisotropic direction.

The specific role of surfactants is described as follows: (1) the unshared pair electrons on the functional head groups of the surfactant strongly interact with the surface atoms of the inorganic species. Since different crystalline surfaces have different atomic arrangements, the adsorption energy of surfactants on different exposed surfaces is different. Therefore, controlled growth of the exposed crystal facets can be achieved by changing the types of surfactants.[83] (2) The deposition of metal atoms on some specific facets can be prevented. The growth process of nanodendrites is rapid, so surfactant molecules are often introduced to stabilize the high-energy crystalline surfaces and can slow down the growth in a certain crystallographic direction.[30,84] (3) Surfactants can coordinate with metal precursors to form stable complexes that effectively modulate the growth habit of inorganic nanomaterials.[85,86] Therefore, it can be noted that the choice of surfactant has an important influence on the structure of the final product. Here, we present the synthesis mechanism of synthesizing nanodendrites using zwitterionic surfactants, cationic surfactants, anionic surfactants, nonionic surfactants and other additives.

2.3.1 Cationic surfactants. Cationic surfactants are the most reported class of surfactants for the synthesis of inorganic nanomaterials. Murphy and coworkers proposed a "zipping" mechanism: the van der Waals stabilization of the surfactant bilayer on the gold surface due to the interchain packing contributes to the formation of the underlying nanorods.[87] In this process, the length of the cetyl trimethylammonium bromide (CTAB) tail is critical to the length-diameter ratio of obtained nanomaterials. Zhu and coworkers proposed that the density of CTAB bilayer distribution on Au nanorods was not uniform, so the experimental conditions can be adjusted to grow Pd nanodendrites at the edges.[88]

Pyridine-based surfactants provide good stabilization to the formed micelles due to the strong π–π stacking between these molecules. For example, Liu and coworkers synthesized branched PdP nanosheets utilizing docosylpyridinium bromide (C_{22}-Py(Br^{-})) as a surfactant, which could self-assemble into lamellar micelles in aqueous solution.[77] As Fig. 3a displays, a strong nanoconfined effect introduced by the lamellar micelles led to anisotropic growth in the crystal plane. In this nanoreactor, the growth outside the crystal plane was strongly suppressed, and the 2D structure was finally obtained. PdIr NDs can also be prepared using this surfactant, and different structures can be extended by varying the type and concentration of halide ions.[89] Poly diallyl dimethyl ammonium

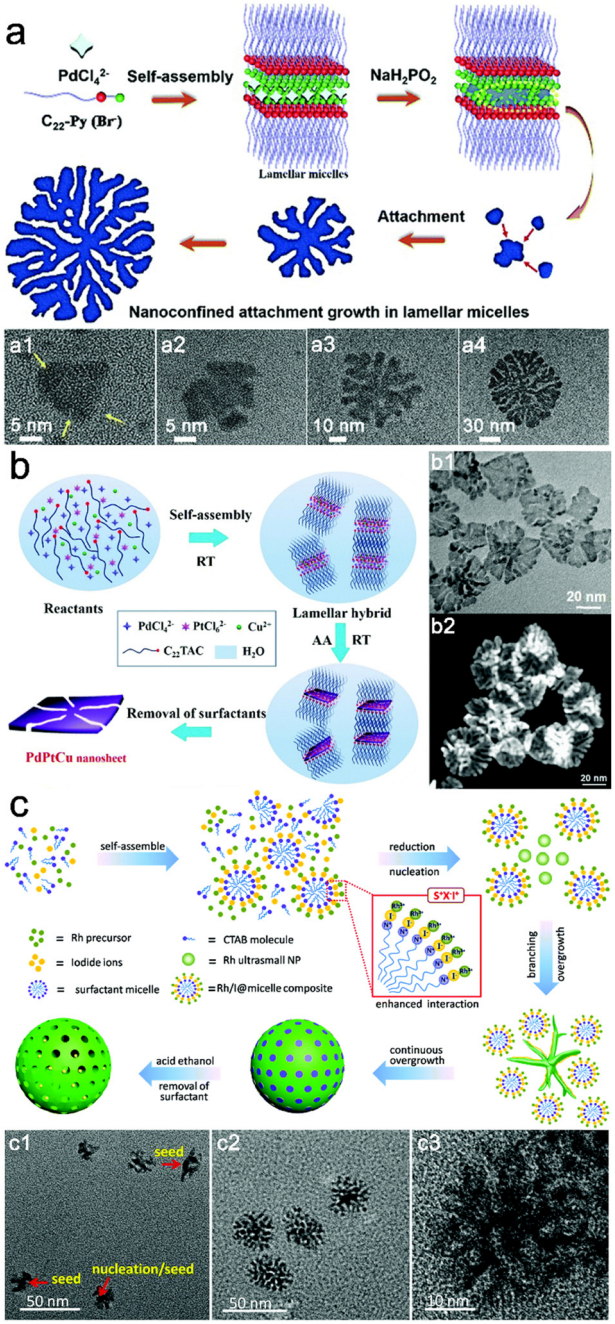

Fig. 3 (a) Schematic illustration of the generation of PdP NSs. a1–a4: typical TEM images obtained from the different growth periods of the ultrathin PdP NSs. Adapted with permission from ref. 77. Copyright 2020, The Royal Society of Chemistry; (b) schematic of the formation of ultrathin free-standing trimetallic PdPtCu nanosheets. b1–b2: TEM and HAADF-STEM image of PdPtCu. Adapted with permission from ref. 78. Copyright 2019, The Royal Society of Chemistry; (c) iodide-mediated templating growth mechanism for the formation of HPRhS. c1–c3: TEM images of the HPRhS sample at different reaction times: 10 min, 15 min, 20 min. Adapted with permission from ref. 79. Copyright 2018, The Royal Society of Chemistry.

chloride (PDDA) and hexadecylpyridinium chloride (HDPC) are also common cationic surfactants used to synthesize nanodendritic materials.[90]

Besides, the heads of cationic surfactants can selectively adsorb on the specific crystal facets of nanocrystals, such as CTAB, which has been reported to preferentially adsorb on the {100} facet of Au seeds.[91] Li and coworkers proposed that octadecyltrimethylammonium chloride (OTAC) could selectively passivate the {110} plane, which can also act as a structure directing agent to ensure the limited 2D nanodendritic growth.[92] Similar surfactants like docosyltrimethylammonium chloride (C_{22}TAC) were used for the formation of ultrathin PdPtCu branched nanosheets (Fig. 3b).[78] Zheng and coworkers studied the detailed formation mechanism of Au nanodendrites.[93] They divided the whole reaction into three stages. In the first stage, Au^0 nucleated immediately by the reduction role of ascorbic acid (AA). The 2,3-diketo-L-gulonic acid (DGA) released during the reduction process and extra decane-1,10-bis(methylpyrrolidinium bromide) ([mpy-C_n-mpy]Br_2) competitively adsorbed on the surface of the Au nuclei and prevented the aggregation. The second stage was the main formation process of dendritic nanostructures. DGA acted as the initial shape-directing agent and formed small branched nanostructures on the surface of Au nuclei. The [mpy-C_n-mpy]Br_2 molecules adsorbed on the surfaces of different nuclei through two headgroups, thus increasing the branching power of DGA and forming the initial branched nanostructures. In the third stage, disordered dendritic nanostructures formed with a slow Ostwald ripening process. Qi and coworkers obtained Au nanodendrites grown along the ⟨211⟩ directions by simply changing the β-cyclodextrin (β-CD)-to-dodecyltrimethylammonium bromide (DTAB) molar ratio.[94]

Cationic surfactants exhibit positive charges and repel each other with some positively charged metal precursors, making it difficult to form organic–inorganic hybrids, which can be well solved if negatively charged halide ions are introduced in the middle position. For example, Qiu and coworkers reported highly porous Rh nanospheres (HPRhS) with the growth mechanism shown in Fig. 3c.[79] The surfactant molecules self-assembled into stable micelles, and the Rh precursor can recombine with the polar heads of micelles through electrostatic action ($S^+X^-I^+$), where the introduced iodide ions replace Cl^- or Br^- to form Rh/I@micelle composites. Due to the stronger chelating ability by the mediation of iodide ions, the interaction between micelles and Rh^{3+} was greatly enhanced. After the addition of the reducing agent AA, Rh/I@micelle was rapidly deposited on seeds in the form of Rh branches. Finally, homogeneous HPRhS was generated through the continuous overgrowth. This is the first example of the synthesis of such a branched structure utilizing chelating interaction.

2.3.2 Anionic surfactant. There are also a few examples of nanodendrites prepared using anionic surfactants alone. Raj and coworkers obtained gold nanoflowers (GNFs) using *N*-2-hydroxyethylpiperazine-*N*-2-ethanesulphonic acid (HEPES) as a reducing/stabilizing agent.[95] In most of the cases, anionic surfactants are used together with other types of surfactants, *e.g.*, cationic surfactants.[96] Moth-Poulsen and coworkers reported Pd nanodendrites using a mixture of CTAB and sodium oleate (NaOL), and they proposed that the addition of

NaOL was able to change the arrangement of surfactants on the Pd seed surface, ultimately leading to a new pattern of growth and aggregation patterns. In addition, the anionic surfactant-sodium dodecyl sulfate (SDS) has also been reported for the preparation of nanodendrites.[97]

2.3.3 Zwitterionic surfactants. The micellar geometries include spheres, ellipsoids, rodlike micelles, wormlike micelles (WLMs), bilayers and vesicles, which can be roughly predicted by the critical packing parameter (C_p)[98] (Fig. 4a). Surfactants with amphiphilic ionic heads are more suitable for the preparation of nanomaterials than ionic analogues with similar hydrocarbon tail group lengths, best explained by the fact that they usually have lower critical micelle concentrations (CMCs). Zwitterionic surfactants are amphoteric due to the dual and opposing charges present in their structure. The advantage is their ability to adsorb on different charged surfaces (cations and anions) without any influence on the total surface charge.[98,99] Lu and coworkers demonstrated that 2,2′-(1,4-phenylenebis(oxy)) bis(*N*,*N*-dimethyl)-*N*-carboxyethyl-*N*-(alkylamide propyl) ammonium chloride (C_{14}-B-C_{14}) displayed different micelles in different pH conditions, where the amphiphile displayed cationic properties in acidic media, forming spherical micelles. In contrast, with the increasing pH, wormlike micelles formed (Fig. 4b).[100] The stable lamellar micelle structure over a wide pH range is beneficial to regulate the experimental parameters for the purpose of preparing 2D nanodendrites.

Shelnutt and coworkers reported the first example of the preparation of single crystal Pt nanodendrites.[57] A single layer of distearoyl-phosphatidylcholine (DSPC) liposomes was used in the reaction, in which the diffusion of metal atoms may be limited. Because the dendrite was sandwiched between two liposomes, the platinum atoms can only diffuse to the edges of the formed nanodendrites and, ultimately, the product behaved as a 2D circular dendritic nanostructure. This work provides the basis for the preparation of more 2D nanodendrites.

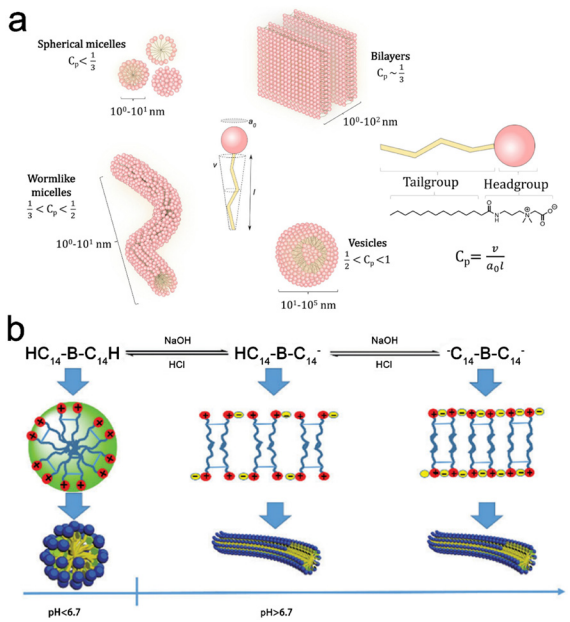

Fig. 4 (a) Self-assembly of zwitterionic surfactants governed by packing parameter. Adapted with permission from ref. 98. Copyright 2021, Elsevier B.V.; (b) simplified diagram of self-assembly behavior transition of C_{14}-B-C_{14} aqueous solution at different pH values. Adapted with permission from ref. 100. Copyright 2022, Royal Society of Chemistry.

Quaternary ammonium-type zwitterionic surfactant not only has the ability to stabilize the lamellar mesophase, but also has another advantage to adsorb on specific crystal facets with the synergetic help of head groups the halogen ions. For example, some halogen ions can selectively adsorb on the {100} facets of fcc Pt NCs, preventing the epitaxial growth of nanocrystals along the {100} facets. Our group reported the preparation of highly branched Pt nanodendrites utilizing $C_{22}H_{45}$-$N^+(CH_3)_2CH_2COOH(Br^-)$ (C_{22}N-COOH(Br^-)), which is a long-chain amphiphilic surfactant with quaternary ammonium and carboxyl functional heads, and halide counterion of Br^- as a structure co-directing agent and co-capping agent.[42] C_{22}N–COOH(Br^-) self-assembled into the nanoconfined lamellar structure and kinetically controlled the in-the-plane epitaxial growth of Pt nanoparticles (NCs) along {110} facets. Finally, Pt NDs with a highly branched structure were obtained, which is the first reported case of ultrathin 2D nanodendrites with such a highly branched structure.

2.3.4 Nonionic surfactants. There are a large number of reports on the synthesis of nanodendrites assisted by nonionic surfactants. The most prominent one remains the study by Yamauchi and coworkers.[101,102] In 2009, they first reported a facile synthetic strategy for dendritic Pt nanoparticles (DPNs) through a block copolymer mediated synthetic strategy. The role of Pluronic F127 in this system was investigated. It was known that the PEO group in Pluronic F127 forms a crown-ethers-like conformation, similar to a cavity structure in an aqueous solution, while the hydrophobic PPO groups facilitate adsorption on the deposited metal surface. The Pluronic chains adsorbed on the Pt surface during Pt deposition form cavities, which further promoted the formation of DPNs.[103] In addition, Pluronic F127 could be replaced by other nonionic surfactants such as Pluronic F127, Brij 700, Tetronic 1107, and polymers such as poly(vinyl pyrrolidone) (PVP) and poly(1-vinylpyrrolidone-*co*-vinyl acetate) (PVP-*co*-VA), which could also yield similar NPDs.[56] Moreover, they were able to fabricate Pt-on-Pd bimetallic nanodendrites with Pluronic P123, with Pd on the inside and dendritic Pt on the outside.[104] Notably, each Pt branch was single crystalline in nature. Besides, in the report by Song and coworkers, the synthesis of 2D circular platinum nanodendrites was also in the presence of P123 as a structural directing agent.[105]

Poly(vinylpyrrolidone) (PVP) can strongly adsorb on metal surfaces through charge transfer interactions between pyrrolidone rings and metal atoms to direct the shape of nanostructures or protect them from agglomeration.[106–109] Wang and coworkers synthesized a multiarmed Pt nanostar with single crystal characteristics.[110] At the beginning of the reaction, a single crystal seed particle was formed. When the Pt(IV) salt was

reduced, the nanostar arms grew. These arms had the same single crystal structure as the initial seed. They concluded that the number of arms on each multi-armed nanostar was determined by the reduction of the Pt(IV) salt around the particle and the rate at which the PVP-360 capping agent capped the particle. Huang and coworkers investigated the effect of different concentrations of PVP on the final product structure.[111] Because PVP does not have the ability to adsorb specific crystal facets, different shapes of products appear under a little content of PVP. However, when the content is too much, it leads to the formation of particles with larger size. Therefore, choosing the suitable concentration is beneficial for the formation of a homogeneous branched structure.

2.3.5 Amino-based and carboxyl-based functional molecules. Due to the strong coordination capability of the NH_2 groups, amino-based surfactants can interact with noble metal precursors to generate NH_2–M^{n+} complexes.[112] Zeng and coworkers found that changing the concentration of octadecylamine (ODA) alone produced two different results.[113] Cu–Pd multi-pods are likely to form when the ODA concentration is under a low level. The reason for this is that the decrease of the capping layer leads to an increase in the atom deposition rate when the high-energy surface grows faster than the low-energy surface, and eventually, anisotropic growth occurs. However, as the ODA concentration increases, the rate of atom deposition decreases to a level that can be significantly regulated by the diffusion of adsorbed atoms, and polyhedral nanocrystals covered by a low index are prepared. In this work, hexadecylamine (HDA), octadecylamine (DDA) and decylamine (DA) were also investigated as capping agents besides ODA. The authors concluded that the stronger steric effect on the binding of Cu–Pd bimetallic nanocrystals diminished, thus favoring dendritic growth. The branched Pt nanostructures were prepared by Yang and coworkers *via* using HDA as a surfactant and reaction solvent with the addition of 1-adamantylcarboxylic acid (ACA) to prevent coordination reactions of the free surface sites with other capping ligands.[114]

Oleylamine (OAm) are common surfactants in solvothermal synthesis reactions, and it is often used in combination with oleic acid (OAc). Tilley and coworkers reported a highly branched Pd nanostructure by altering the nature of the organic stabilizer system.[115] In this work, the difference in the surface stability from OAm and OAc functional groups determined the growth kinetics. OAc binds weakly to Pd, thus reducing the overall degree of surface stability and resulting in branching growth. They proposed three distinct growth stages for the formation of highly branched Pd. In the first stage, the ratio of OAc to OAm is 1 : 1. The growth process of this reaction stage was relatively slow and thermodynamically tends to form multiple twinned fcc icosahedral nuclei. In the second stage, the reaction was two times faster than stage-I and kinetically growth dominated, resulting in branched growth from the twinned nuclei. However, there was still limited growth along selected crystal orientations until stage-III was reached, which get rid of growth along specific crystal facets and gives a highly branched morphology. Therefore, the selection of a suitable surfactant with selective binding ability can change the growth kinetics by changing the coalescence rate.

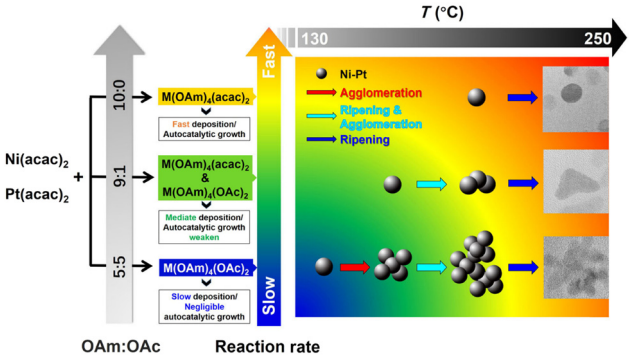

Fig. 5 The structural controlling mechanism for Ni–Pt NPs. With different OAc concentrations, precursors take varied reaction pathways. In the meantime, the reduction temperature depends on the ratio between OAm and OAc. Once the precursors are reduced into Ni and Pt atoms, the nucleation process begins. The growth mechanism after nucleation varies along with different reaction rates. Under rapid deposition and growth, Ostwald ripening predominates, while at a lower rate, particle agglomeration plays a higher part. Hence differently shaped seeds and outgrowth particles are synthesized. Adapted with permission from ref. 116. Copyright 2020, Tsinghua University Press and Springer-Verlag GmbH Germany, part of Springer Nature.

OAm/OAc surfactant mixtures also play a key role in reducing the initial temperature of Pt reduction nucleation and preferential passivation of the {111} facet.[116–118] Lau and coworkers depicted a structural controlling mechanism by altering the molar ratio of OAm/OAc, reaction temperature and reaction pathways (Fig. 5). In the absence of OAc, the nucleation of nickel and platinum required a processing temperature higher than 200 °C and the products were nanoparticles. With the presence of OAc in the solution (OAm : OAc = 9 : 1), some metal–ligand complexes turned into $M(OAm)_4(OAc)_2$. Under this condition, the nucleation temperature dropped below 200 °C because of the reducing nature of OAc. When more OAc was added (OAm/OAc = 1 : 1), the nucleation of Pt was facilitated at a relatively low temperature of 130 °C, and the petals-like nano-nuclei cluster tend to form flower-like branched structures. It is not difficult to find that another surfactant often exists in the OAm system to prevent the aggregation of nanoparticles and nanodendrites during the growth stage. For example, Li and coworkers synthesized Pt–Ni nanodendrites using OAm as a surfactant and OAc as a co-surfactant, respectively. In addition, didodecyldimethylammonium bromide (DDAB) was also applied to improve the dispersion of the nanodendrites.[119,120] Feng and coworkers reported the synthesis of PdM (M = Pt, Co, Ni) nanodendrites using OAm as a surfactant and verified the co-stabilizing role of HDPC in the synthesis process.[121]

In addition, carboxyl-based functional molecules are common structure-directing agents. Formic acid plays a dual role in the synthesis of PDNs as a reducing agent and a structure directing agent.[122] Liu and coworkers reported that the carboxylic groups in formic acid and sodium citrate adsorbed on

specific crystal facets of the Pt surface, resulting in different growth rates on different crystal facets and finally the successful preparation of the Pt multipod.[123] AA is a commonly used reducing agent in the preparation of noble metals due to its relatively gentle reducing ability, and its oxidation product of AA is DGA. Yamauchi speculated that DGA with carboxyl functional groups acts as a capping agent for Pt{100} and {110} facets, guiding their growth along {111} facets.[124] Sodium *N*-(4-*n*-dodecyloxybenzoyl)-L-isoleucinate (SDBIL) was used as functional molecules to synthesize Au, Pd and Pt dendritic nanostructures with pH-dependent self-assembly properties.[125] SDBIL forms different micellar structures under acidic and alkaline conditions, for instance, vesicles in alkaline pH (7.0–8.5) and fibrillar structures in acidic solution (5.0–6.0). Thus, the structure of the product can be tailored by adjusting the pH values.

2.4 Chemical etching growth

The chemical etching method involves the use of some chemical reagents to etch the atoms of the generated structures, which can be prepared by changing the experimental parameters to achieve controlled etching of some complex architectures. It mainly includes galvanic replacement and oxidative etching reaction, and the frequently used etching agents are $NH_3{\cdot}H_2O$, $Fe(NO_3)_3$, Fe^{3+}/Br^-, H_2O_2, Cl^-/O_2, *etc.*[126–129] For example, Chen and coworkers synthesized Pt–Cu nanodendrites with small amounts of additives (*i.e.*, $FeCl_3$ and HCl).[130] These additives, synergy with O_2 in the air, can serve as oxidative etchants, react with the reduced Pt and Cu atoms to return them to the oxidized form, and thus realize the etching. Additionally, Yang and coworkers proposed that the proton or H^+ plays a key role in accelerating such an etching process.[131]

I^- acting as a capping agent strongly adsorbs on the {100} facet of the noble metal nanocrystals to form {100}-enclosed nanocrystals.[132] Besides, it can also form a NaI/I_2 mixture with NaI, and this mixture can be used as an etching agent to obtain hierarchical Pt–Cu superstructures (Fig. 6a).[133] There are two relatively important stages in the whole experimental process. The first is the decomposition of CuI and the reduction of I^- *in situ* release I_2, which can etch the resulting structure. The etching rate is determined by the amount of I^-. Secondly, the generated Cu^0 can undergo a galvanic replacement reaction with Pt^{4+}. Wang and coworkers suggest that both oxidative etching and galvanic replacement reaction play an important role in the generation of branched structures.

Oxidative etching in electrochemical processes has also been reported. Tang and coworkers reported that selective oxidative etching of Cu atoms by Pt–Cu nanocatalysts is the key to the formation of nanodendritic morphologies.[134] Pt is an effective electrocatalyst towards oxygen reduction reactions, where dissolved oxygen in water is reduced on the surface of PtCu nanocrystals. In this process, Cu atoms act as electron donors and are selectively oxidized back to Cu^{2+} species by O_2 and dissolved into the solution, eventually forming the nanodendritic structure (Fig. 6b). The importance of O_2 is demonstrated by the fact that no oxidative etching reaction occurs when N_2 is used instead of O_2.

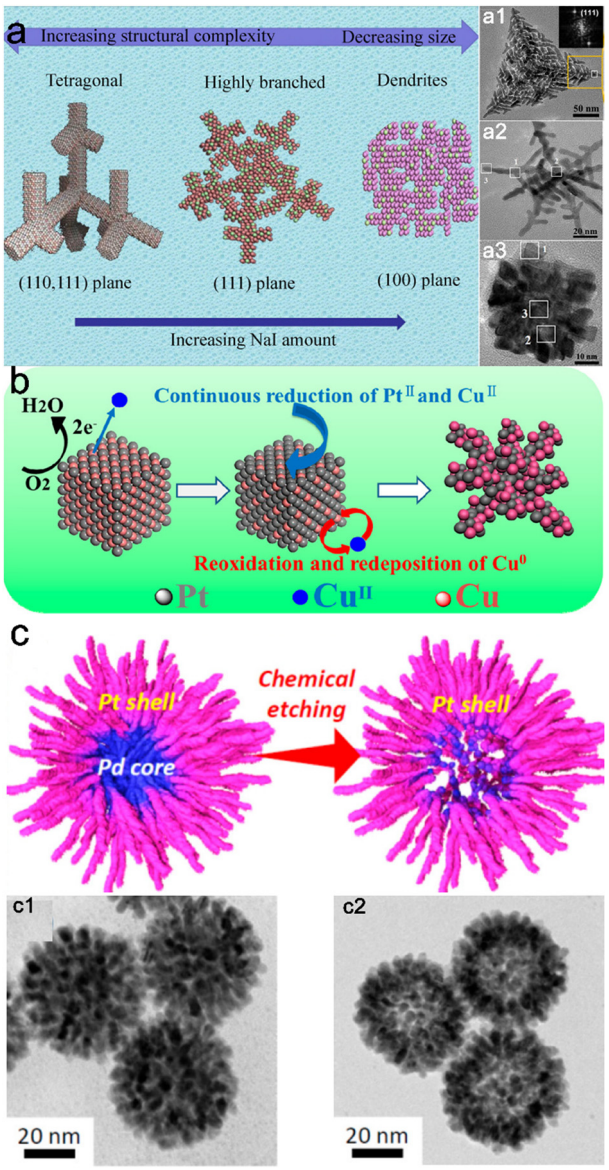

Fig. 6 (a) Schematic illustration of the controlled growth of 3D hierarchical Pt–Cu superstructures. a1–a3: TEM image of Pt–Cu tetragonal, highly branched and dendrites, respectively. Adapted with permission from ref. 133. Copyright 2014, Tsinghua University Press and Springer-Verlag Berlin Heidelberg; (b) progressive formation of Pt–Cu BANDs. Adapted with permission from ref. 134. Copyright 2014, American Chemical Society; (c) schematic presentation for the formation of bimetallic dendritic nanocage with a hollow interior and porous dendritic wall. c1–c2: TEM images for dendritic Pt-on-Pd nanoparticles before chemical etching dendritic nanocages after chemical etching. Adapted with permission from ref. 135. Copyright 2013, American Chemical Society.

Nitric acid can also be used as an etchant due to the difference in chemical stability of different metals. For example, Yamauchi and coworkers synthesized bimetallic Pt–Pd hollow nanoparticles with dendritic shells through the selective chemical etching method.[135] The Pd core can be etched by nitric acid (14 M), while the Pt exterior shell is relatively stable

and thus retained (Fig. 6c). This method does not completely etch the Pd core, and a part of Pd forms a PdPt alloy with Pt at the interface. The choice of the etching agent with the appropriate strength is the key to obtain nanocrystals with an optimal structure.

2.5 Other growth models

2.5.1 Electro-deposition growth. Electro-deposition is widely used in the field of nanomaterials due to its simple operation and good controllability. The morphology of the target product can be adjusted by regulating the experimental parameters, such as applied potential, electrolyte and its concentration, electrodeposition time, *etc.*[136,137] For example, Shao and coworkers reported Ag dendritic nanostructures obtained by electro-deposition, where the morphology of the Ag nanostructure could be regulated by electrolysis time, working electrode potential and Ag ion concentration.[138,139] However, the disadvantage of electro-deposition is also obvious, that is, the prepared products are difficult to have the characteristics of ultrathin and ultrasmall.

2.5.2 Hard templated growth. Silicon dioxide (SiO_2) nanospheres are commonly used as a hard template because of their homogeneous shape and easy removal. Lee and coworkers reported Pt-on-Au nanodendrites by Au-seed-mediated growth inside hollow silica nanospheres, where hollow SiO_2 act as a nanoreactor. The products prepared by this method are ligand-free and can be scaled up to gram scale reactions.

Xie and coworkers used RANEY® nickel as a hard template and reducing agent to prepare Pd and Ag dendritic nanostructures under ultrasound assistance. This strategy has two unique advantages: first, the whole reaction process can be carried out at room temperature and pressure; second, the RANEY® nickel template is much easier to remove than other hard templates because of its rapid reaction with dilute hydrochloric acid (HCl) solution.[140]

2.5.3 Microwave-assisted growth. A microwave-assisted chemical reaction can produce highly crystalline fcc multipod structures in a few minutes. The application of single-mode cyclic microwave heating has been shown to enhance the growth of (111) planes to form multipod nanoparticles with large aspect ratios.[141] Meng and coworkers synthesized reduced graphene oxide supported Pt nanodendrites by a microwave-assisted simultaneous reduction.[142] The Pt nuclei were anchored to the surface of graphene oxide (GO) by forming Pt–O linkages with the oxygen-containing functional groups on GO.

2.5.4 SLS transformation growth. Bao and coworkers proposed a solid–liquid–solid (SLS) transformation growth mechanism for growing dendritic Pd nanostructures.[143] This growth mechanism is similar to the chemical etching mechanism. In this work, polyglycols act as a structure-directing agent while hydrazine as a reducing agent. A large excess of hydrazine dissolved the initial Pd particles and Pd atoms redeposited on the structure to form the dendritic Pd nanoparticles.

2.5.5 Electron beams mediated growth. The rapid development of *in situ* electron microscopy has undoubtedly been a catalyst for the development of nanocatalysts, allowing us to directly observe the growth process of nanodendrites.[144] The electron beam can be used directly as a reducing agent to reduce noble metals.[145] *In situ* liquid-cell transmission electron microscopy (LC-TEM) recorded the formation of nanoclusters, the transformation of nanoclusters to multi-branched structures, and the splitting tips into hyper-branched dendrites. Zheng and co-workers pointed out that the branch and dendritic growth were related to the curvature and growth rate of the tip (Fig. 7a).[146] Jin and coworkers found that the initial transition from nanoclusters to multi-branched nanostructures was due to interfacial instability caused by supersaturation under a limited supply of monomers for diffusion (Fig. 7b).[35] Multi-branched nanostructures provide multiple nucleation sites, leading to the emergence of superbranched dendrites. This is due to the influence of precursor/monomer depletion and diffusion fields, which is related to precursor concentration and electron dose rate. *In situ* observations show that the newly formed nanoclusters first transform into

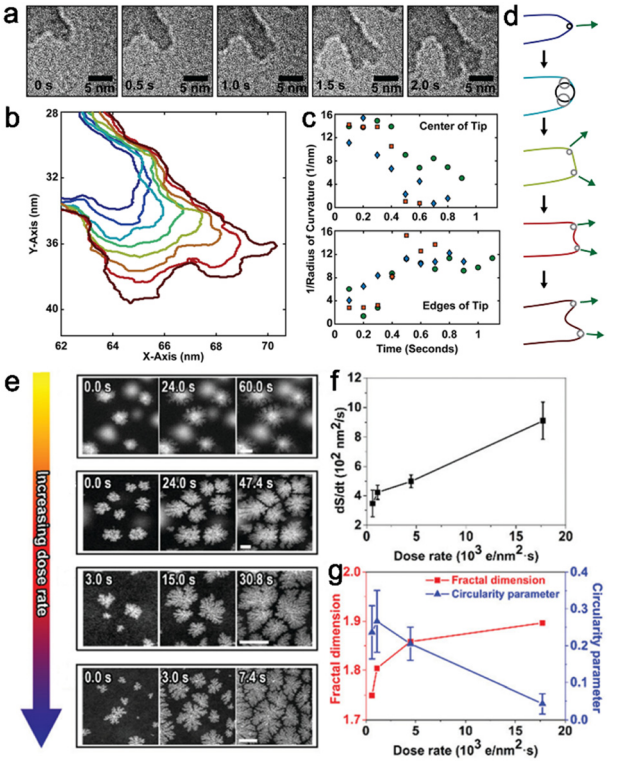

Fig. 7 (a) Sequential images showing a tip split into two equivalent new tips growing into two branches; (b) outlines of the splitting tip in part a. The original single tip (blue) widens and grows on the corners of the flattened top (red); (c) measured curvature at the center and edges of the tip during the splitting process; (d) schematic showing the tip splitting process. Adapted with permission from ref. 146. Copyright 2018, American Chemical Society; (e) *in situ* HAADFSTEM images of the Pd nanocrystal growth process at different electron dose rates: 0.61×10^3 e nm^{-2} s^{-1}; 1.12×10^3 e nm^{-2} s^{-1}; 4.47×10^3 e nm^{-2} s^{-1}; and 1.77×10^3 e nm^{-2} s^{-1}; (f) average projected area change (dS/dt) of Pd nanocrystals as a function of the electron dose rate; (g) Fractal dimensions and circularity parameters *versus* electron dose rates. Adapted with permission from ref. 35. Copyright 2019, The Royal Society of Chemistry.

multi-branched nanocrystals and then eventually evolve into dendrites. Increasing the rate between atomic formation/incorporation and diffusion accelerates the formation and growth of dendritic structures. Therefore, the fractal dimension of nanocrystals can be adjusted by the degree of supersaturation, which opens a new window to explore the relationship between supersaturation and crystal morphology in materials science.

3. Synthetic approaches for noble metal nanodendrites

With the development of nanoscience and synthetic chemistry, there are abundant new synthetic methods, making it easy to break strong metal bonds and symmetries. Over the past two decades, researchers have devoted themselves to the synthesis of nanomaterials with various crystal structures, morphologies and compositions. Generally speaking, well-defined nanostructures tend to exhibit superior performances, particularly in nanodendritic structures. The merits of nanodendrites include the abundant steps, cavities, a large number of unsaturated coordination atoms, and the high proportion of tips exposed by dendritic structures. These characteristics have stimulated the enthusiasm of researchers for further research in this field. The growth mechanism of anisotropic noble metal nanocrystals has been discussed in detail in the previous chapter. In this chapter, we have chosen some representative examples to discuss the synthetic approaches. This section is divided into two subsections, 2D and 3D nanodendrites.

3.1 Two-dimensional nanodendrites

2D nanomaterials are characterized by high aspect ratios, unique surface chemistry, and quantum-size effects that endow the nanomaterials with unusual physicochemical properties.[147] However, because of symmetry-breaking events and high surface energy, 2D morphologies of noble metals are thermodynamically unfavorable.[105,148] Many methods have been reported for noble metal 2D materials, including hydro-/solvothermal methods and seeded methods. These experiences can be borrowed to prepare 2D dendritic nanostructures, and the branched growth can be obtained by adjusting the experimental parameters. The major difference between hydrothermal and solvothermal reactions is that the former uses water as a solvent while the latter is an organic solvent. By adjusting parameters such as temperature, pressure and concentration and type of precursors, the characteristics of the crystalline phase and crystal structure can be changed. These two methods have become the mainstream strategy for the synthesis of nanodendritic structures due to their simplicity, low cost, and one-step synthesis of morphologically homogeneous products. However, the disadvantages of these two methods are also obvious, such as the difficulty in scaling up production and the organic substance in the reaction system, such as long-chain surfactants, which can hinder the *in situ* observation of the growth mechanism.

In 2004, Shelnutt and coworkers found that 2D nanodendrites could be produced when large liposomes were used.[57] In this work, unilamellar DSPC liposomes with a diameter of 160 nm were used in the reaction, mixed with aged Pt complex and AA solution and irradiated with incandescent light for 30 min. The reaction solution turned black and 2D Pt nanodendrites were generated. The reaction rate was dependent on the irradiation intensity and the surfactant assembly size. As shown in Fig. 8a, TEM images of the product exhibit the 2D circular nanostructures with a thickness of about 2 nm.

Chen and coworkers reported 2D PdAg alloy nanodendrites in 2018.[92] PdAg NDs were carried out by the co-reduction reaction of Pd and Ag precursors in aqueous solution using octadecyltrimethylammonium chloride (OTAC) as the structural directing agent and AA as the reducing agent. The OTAC and precursor mixture was bath-sonicated for 10 min, followed by the addition of the reducing agent. The reaction was reacted at 20 °C for 2 h without stirring. Different compositions of PdAg alloys can also be obtained by varying the feeding molar ratios. TEM images revealed that the final product was 2D nanodendrites with an average lateral size of ~80 nm, and elemental mapping supported the formation of uniform PdAg alloy (Fig. 8b and c). Atomic force microscopy (AFM) showed a thickness of ~5 nm and slightly thicker branches of ~7 nm (Fig. 8d). This method can also be extended to prepare ternary PdAgPt nanowheels with 2D dendritic structures (Fig. 8e–g).[149]

Our group designed a long-chain amphiphilic surfactant (C_{22}N-COOH(Br^-)) and prepared Pt NDs in a facile one-step approach in aqueous solution.[42] In this work, H_2PtCl_6 is used as the precursor and AA is used as the reducing agent. The reaction was kept at 50 °C for 12 h. We precisely engineer the Pt NDs generation from Gen 0 (2 nm) to Gen 25 (500 nm) by changing the reactants conditions (*e.g.*, H_2PtCl_6, AA and H_2O). This method can also be utilized to grow other noble metal NDs (PdNDs and AuNDs) and core–shell Pt@Pd NDs. TEM image of an individual Gen-7 Pt ND in Fig. 8h displays a highly branched structure with an average diameter of ~150 nm and the branches along the planar directions are in the range of 2–4 nm. Most importantly, the thickness of Pt NDs prepared by this method is only 2.3 nm (Fig. 8i). The method could also be extended to the bimetallic system PtRu, PtAg, PtRh, *etc.*[150] The obvious difference between the monometallic Pt NDs and bimetallic alloys is the thinner thickness of the alloy. This result can be explained by the fact that the reduction process of the two precursors was disturbed to some extent due to the different reduction electrode potentials of the two metals, and the reduction of Ru in the system reduced the atomic stacking rate, and the thickness of the prepared PtRu NDs was only ~1.8 nm (Fig. 8j and k).

The currently reported preparations of 2D nanodendrites require AA as a reducing agent. Because the reducibility of AA is neither too strong nor too weak, which can ensure both the slow reduction of noble metals and the subsequent rapid growth.[84] All of the above studies are on the preparation of nanodendrites in the aqueous phase, but some examples have also been reported in the oil phase. For example, Huang and

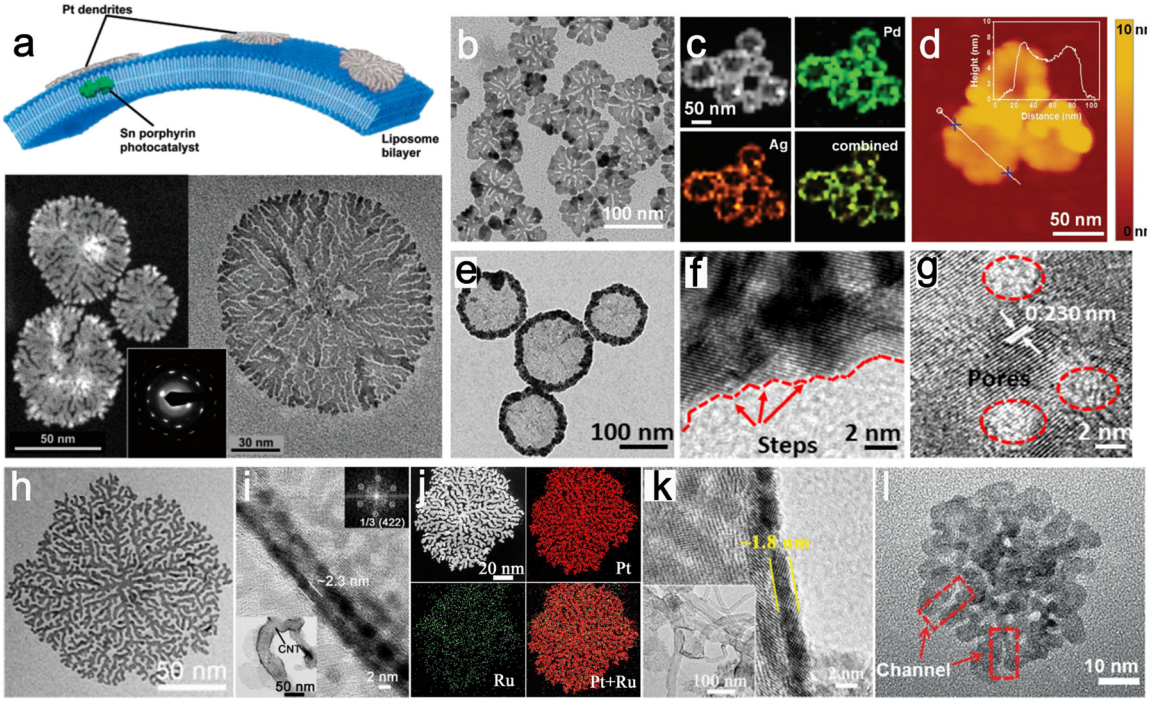

Fig. 8 (a) Illustration of the growth of Pt nanosheets on the liposomal surface and HAADF scanning TEM image of a large dendritic Pt nanosheet (inset: Its electron diffraction pattern). Adapted with permission from ref. 57. Copyright 2004, American Chemical Society; (b) low-resolution TEM images of 2D PdAg NDs; (c) STEM image and corresponding elemental mapping of Pd and Ag; (d) AFM image and corresponding height profile across a 2D PdAg nanodendrite. Adapted with permission from ref. 92. Copyright 2018, Wiley-VCH Verlag GmbH & Co. KGaA, Weinheim; (e) TEM and (f and g) HRTEM image of $Pd_{43}Ag_{21}Pt_{36}$ nanowheels. Adapted with permission from ref. 149. Copyright 2020, American Chemical Society; (h) TEM and (i) HRTEM images taken from the cross section of a Pt ND which stands vertically on the TEM grid assisted by CNTs (the inset in the top right is the corresponding Fourier diffractogram. Adapted with permission from ref. 42. Copyright 2019, American Chemical Society; (j) TEM and (k) HRTEM images taken from the cross section of a Pt–Ru ND that was standing vertically on the TEM grid, The adoption of this orientation of the ND was assisted by CNTs (inset in the bottom left). Adapted with permission from ref. 150. Copyright 2019, The Royal Society of Chemistry; (l) high-magnification TEM image of RuCu NSs. Adapted with permission from ref. 151. Copyright 2019, Wiley-VCHVerlag GmbH &Co. KGaA, Weinheim.

coworkers reported the preparation of channel-rich RuCu nanosheets in the oil phase with $RuCl_3 \cdot xH_2O$ and $CuCl_2 \cdot 2H_2O$ as precursors, phloroglucinol as the reducing agent, and OAm and octadecene as a mixed solvent.[151] Since the migration rate of the precursors was slow in the oil phase solvent, the corresponding reaction temperature needed to be increased to 210 °C. The TEM images of the nanodendrites are shown in Fig. 8l, with an average size of 48.7 nm, a thickness of about 6 nm, and a large number of accessible channels in the structure. There are still relatively few reports on the preparation methods of 2D nanodendrites and their applications, so there are still more possibilities to be explored in the preparation of 2D nanodendrites.

3.2 Three-dimensional nanodendrites

Generally speaking, 3D nanodendrites do not require confined-limited growth along the planar direction, so their synthesis conditions are relatively wider compared to 2D nanodendrites. The synthesis approaches of 3D nanodendrites have been extensively studied, such as hydro-/solvothermal methods,[152] seeded methods,[153] electro-deposition methods and hard templated methods, *etc.* It is not difficult to find some well-defined 3D nanodendrites mainly using hydro-/solvothermal method. The advantages and disadvantages of this method have been discussed in the previous section. The advantage of seeded methods is that one can select any existing nanocrystals as a seed and add precursors, reducing agents and/or surfactants to obtain nanodendrites with a variety of new shapes. Accordingly, the disadvantages of the method are that the degree of lattice mismatch between the subsequently grown noble metals and the nucleus metal interferes with the subsequent growth and that a separate reduction of the second metal is inevitable during the growth process. Therefore, the seeded method has many limitations for practical applications. The electrodeposition method utilizes a two- or three-electrode system with a noble metal precursor as the electrolyte to reduce the noble metal salt from the oxidized form to the metallic state and thereby deposit it onto the electrode surface. The electrodeposition method is simple, and the structure and chemical composition of the deposited material can be controlled by controlling the pH of the electrolyte, potential or current density, the concentration of the electrolyte and the deposition time, making it suitable for industrial large-scale production. However, its disadvantage is that the precise controllability is poor, and it is difficult to obtain well-defined nanodendrites, so the electrocatalysis performance of the resulting samples is

poor. The hard-template method uses a rigid nanomaterial as a template to act as a "micro-reactor", and noble metal materials are grown on the surface to replicate the structure of the hard template. The resulting nanodendrite structure usually has a narrow particle size distribution. However, this method is less used in the field of nanodendrite preparation because it tends to destroy the nanomaterial structure and introduce impurities when removing the hard template. A large amount of work has been reported, and we selectively summarize representative examples in recent years.

Strasser and coworkers presented the synthesis of nanostructured iridium nanodendrites (Ir-ND) supported on antimony doped tin oxide (ATO).[154] Under the strong reducing ability of $NaBH_4$, a large amount of Ir seeds were first generated, followed by attachment guidance with tetradecyltrimethylammonium bromide (TTAB), and finally branched Ir NDs were obtained with a narrow size range of 15–20 nm. Huang and coworkers reported the preparation of $PdH_{0.43}$ nanodendrites by a one-pot synthesis.[155] It was obtained by dissolving palladium(II)acetylacetonate ($Pd(acac)_2$) and *n*-butylamine in *N*,*N*-dimethylformamide (DMF) and heating at 160 °C for 4 h. The characterization results showed that the as-synthesized $PdH_{0.43}$ nanodendrites still maintained the fcc structure. Chen and coworkers also proposed a method for the preparation of PdH-NDs, with the difference that they used a two-step synthesis.[156] Pd NDs were first grown as seeds. Subsequently, the Pd NDs seeds were dispersed in the DMF solution and reacted at 160 °C for 20 h. The H atoms were derived from successive chemical H intercalations in DMF. After centrifugation and washing, PdH-NDs were obtained.

Guo and coworkers reported IrW NDs which were synthesized using iridium(III)chloride hydrate ($IrCl_3{\cdot}xH_2O$) and tungsten carbonyl ($W(CO)_6$) as metal precursors, OAm as the solvent, cetyltrimethylammonium chloride (CTAC) as the surfactant, and glucose as a reducing agent.[157] The mixture was then heated at 250 °C for 3 h. Fig. 9a and b show that IrW NDs exhibit a highly porous nanostructure with a size of 25 ± 2 nm and a surface containing atomic steps and kinks. Zhang and coworkers designed a method for selective epitaxial growth of Ir on as-synthesized hexagonal close-packed (2H) Pd seed.[158] In this synthesis, the Pd seeds were first dispersed in the OAm solution followed by the addition of iridium(III)acetylacetonate ($Ir(acac)_3$). The reaction solution was evacuated for 20 min and then purged with N_2. After dissolving $Ir(acac)_3$ at 110 °C, the reaction increased to 190 °C for 10 hours. As a result, fcc-2H-fcc heterophase $Pd_{66}@Ir_{34}$ nanoparticles were formed. By extending the reaction time, the Ir branch can be further grown to form 3D nanodendrites ($Pd_{45}@Ir_{55}$ nanodendrites). TEM images in Fig. 9c reveal that the $Pd_{45}@Ir_{55}$ nanodendrites possess a 3D multibranched architecture with an average size of 13.2 ± 2.0 nm, and the HAADF-STEM image and corresponding FFT patterns of a representative $Pd_{45}@Ir_{55}$ nanodendrite (Fig. 9d and insets f_1 and f_3) demonstrate the growth of fcc-Ir branches on two opposite sides with unconventional 2H-Ir branches in the middle of 2H-Pd seed (inset f_2 of Fig. 9d). Wang and coworkers synthesized PtPdRu PNDs by ultrasonic

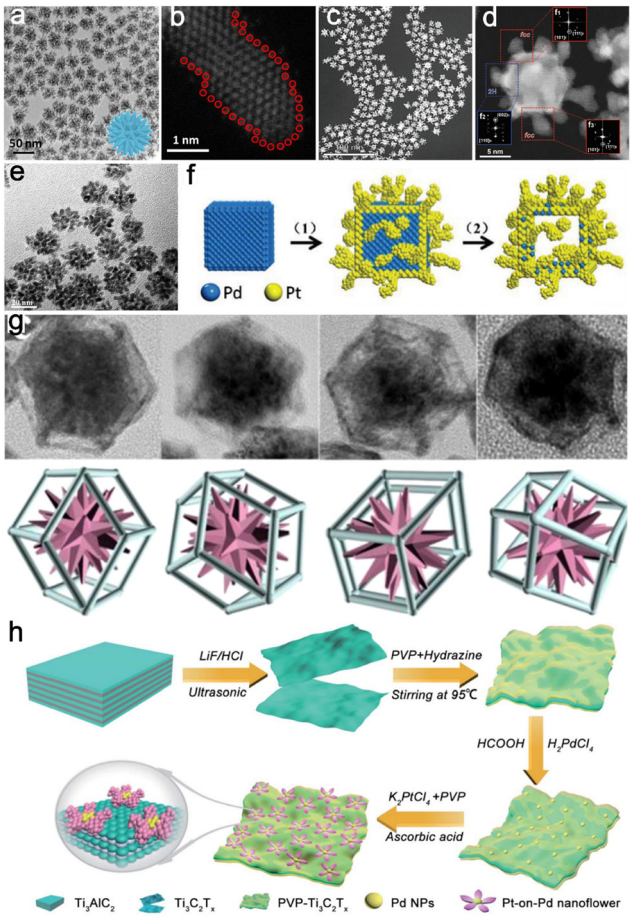

Fig. 9 (a) TEM and (b) HAADF-STEM of IrW nanodendrites. Adapted with permission from ref. 157. Copyright 2018, American Chemical Society; (c) STEM image and (d) HAADF-STEM image of a typical fcc-2H-fcc heterophase $Pd_{45}@Ir_{55}$ nanodendrite. Insets f_1–f_3: the corresponding FFT patterns taken from the red dashed areas (f_1 and f_3) and the blue dashed area (f_2). Adapted with permission from ref. 158. Copyright 2021, Wiley-VCH GmbH; (e) high magnification TEM image of the PtPdRu PND. Adapted with permission from ref. 159. Copyright 2017, The Royal Society of Chemistry; (f) schematic showing the major steps involved in the synthesis of Pt hollow nanodendrites. Adapted with permission from ref. 160. Copyright 2018, Wiley-VCH Verlag GmbH & Co. KGaA, Weinheim; (g) TEM images and models at different angles of Pt–Co ND–NF. Adapted with permission from ref. 161. Copyright 2020, Elsevier B.V.; (h) schematic of the preparation of the Pt-on-Pd/$Ti_3C_2T_x$ hybrid. Adapted with permission from ref. 166. Copyright 2021, The Royal Society of Chemistry.

treatment of three metal precursors at room temperature with AA as a reducing agent and PVP as a structure directing agent.[159] As shown in Fig. 9e, the PtPdRu PNDs have an average diameter of ~21 nm and a well-defined porous dendritic structure with multi-branches. Ge and coworkers prepared Pt hollow nanodendrites by a two-step method.[160] Firstly, PVP was mixed with AA and KBr in the aqueous solution at 80 °C, then Pd precursor was added and continued by heating the reaction at 80 °C for 3 h to obtain Pd nanocubes. The Pd nanocubes were washed and redispersed into ethylene glycol solution as the seed solution for the next reaction step. Second, Pd seeds, PVP, AA, and KBr were dissolved into 30 mL of ethylene glycol

solution at 110 °C with stirring for 1 h. Then, the Pt precursor was added at a controlled flow rate and the reaction was carried out at 190 °C until the Pt precursor was completely injected. Then, when cooled to room temperature, Pt atoms are first selectively deposited on the prefabricated Pd nanocubes and grow into abundant branches to generate Pd@Pt core-frame nanodendrites (Fig. 9f). Finally, the Pd core was etched into the Pt hollow nanodendrites by oxidative etching.

Due to the unique structural characteristics of nanodendrites, the corresponding composite nanomaterials are also considered to be promising. Shen and coworkers reported the first synthesis of self-etched Pt–Co nanodendrites within nanoframes (Pt–Co ND–NF) by a simple one-pot approach (Fig. 9g).[161] They proposed that the amount of water, the ratio of mixed solvent OAm to OAc, and the amount of surfactant hexadecyl trimethyl ammonium bromide were critical factors affecting the formation of the nanostructure. In addition, there are many reports about GO loaded nanodendritic structures.[162–165] This is because the GO structure is rich in oxygen-containing functional groups, such as –OH, –COOH and epoxy, and it can serve as a reducing agent to produce highly dispersed nanodendrites.

In recent years, 2D transition metal carbides (MXenes) can also be used as a carrier due to their metallic conductivity and atomic thickness. Li and coworkers reported the synthesis of 3D porous Pt-on-Pd bimetallic nanodendrites on a 2D ultrathin $Ti_3C_2T_x$ MXene matrix (Pt-on-Pd/$Ti_3C_2T_x$).[166] As shown in Fig. 9h, 2D $Ti_3C_2T_x$ nanosheets were first obtained by etching commercial Ti_3AlC_2 powders in LiF/HCl solution. Second, the $Ti_3C_2T_x$ surface was modified with PVP to obtain PVP-functionalized $Ti_3C_2T_x$ nanosheets. Then, it was used as a carrier to support the subsequent reduction of Pd precursors to generate Pd nanoparticles. Finally, Pt precursors were reduced with the help of AA to finally form the Pt-on-Pd/$Ti_3C_2T_x$ nanoarchitecture.

4. Applications of noble metal nanodendrites

The diverse synthesis approaches of nanodendrites materials allow them easy to maneuver their physicochemical properties, which leads to a wide range of applications, such as biosensors,[167–170] batteries,[171] organic catalyses,[172–174] electrochemiluminescence (ECL) and others.[175–181] Here, we mainly summarize the extensive utilization of nanodendrites in electrocatalysis. In addition, biosensing and therapeutic applications are also briefly described.

4.1 Electrocatalysis

Electrocatalysis refers to the reduction of the activation energy (E_a) in a catalytic reaction by introducing a catalyst, which involves the interaction between the catalyst and the catalytic reaction intermediates. The electrocatalytic reaction occurs on the surface of nanocatalysts, so the structure of the catalyst with its surface atomic arrangement contributes to a certain extent

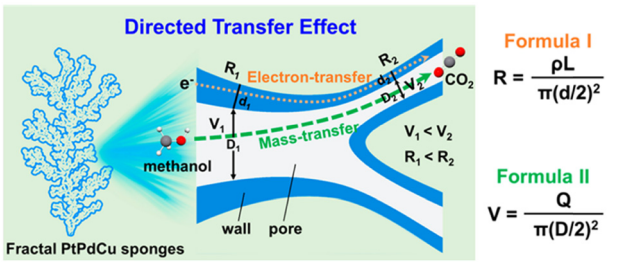

Fig. 10 Scheme illustration of the directed mass- and electron-transfer effect mechanism in PtPdCu–HS. Adapted with permission from ref. 182. Copyright 2021, American Chemical Society.

to how well the electrocatalysis performs. In this section, we emphasize the importance of the nanodendrites structures in optimizing the activity of noble metals for electrocatalytic reactions (*e.g.*, HER, ORR, MOR, EOR, FAOR, CO_2RR).

To elucidate the relationship between the structural design and functional enhancement of dendritic electrocatalysts, Yang and coworkers proposed a new concept and mechanism for directed mass and electron transfer on the micro/nanoscale by establishing a PtPdCu model (Fig. 10).[182] The main contents are as follows: (1) the wall of the main pore is thicker than the wall of the sub pore (d1 > d2), so the electrical resistance of the main pore wall is smaller than that of the sub pore (R1 < R2) according to Formula I in Fig. 10. This will facilitate the oriented transfer of electrons from the main pore to the sub pore. (2) According to formula II, the size of the sub pore is smaller than that of the main pore (D1 < D2) and the mass transfer rate in the sub pore will be faster than that of the main pore (V1 > V2). It is concluded that dendritic structure leads to the exposure of the more active sites and higher mass/electron transfer accessibility. Practical applications of nanodendrites have been reported, for example, Steinberger-Wilckens and coworkers synthesized PtPd NDs as a cathode for H_2/air polymer electrolyte fuel cells (PEFC).[183] The doping of Pd not only helps to influence the final morphology but also greatly reduces the mass transfer resistance, so it exhibits higher power performance. Therefore, there are more possibilities for nanodendrites in the field of electrocatalysis to be explored.

4.1.1 Hydrogen evolution reaction (HER). HER is considered as a feasible method for producing high purity hydrogen from water (HER, $2H^+ + 2e^- \rightarrow H_2$). Two catalytic mechanisms exist for the HER, the Volmer–Heyrovsky (V–H) mechanism and the Volmer–Tafel (V–T) mechanism. Taking acidic conditions as an example, the first step is that the electron from the electrode surface captures a proton and forms H_{ads} on the active site of the catalyst: $H^+ + e^- \rightarrow H_{ads}$ (Volmer step). The difference between the two catalytic mechanisms lies in the second step. In the V–H mechanism, H_{ads} coverage is low and tends to combine with protons to release H_2: $H_{ads} + H^+ + e^- \rightarrow H_2$ (Heyrovsky step); whereas in the V–T mechanism, H_{ads} coverage is high, and two adjacent H_{ads} combine to evolve H_2: $H_{ads} + H_{ads} \rightarrow H_2$ (Tafel step). The reaction mechanism under alkaline conditions is as follows: $H_2O + e^- \rightarrow H_{ads} + OH^-$ (Volmer step); $H_2O + H_{ads} + e^- \rightarrow H_2 + OH^-$ (Heyrovsky step);

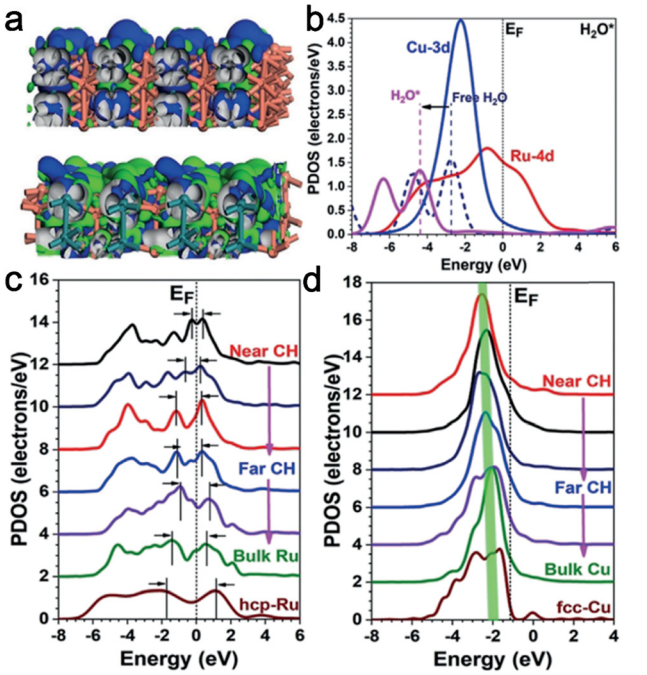

Fig. 11 (a) The side views of the real-spatial contour plots for the bonding and anti-bonding orbitals near E_F of the pristine RuCu NPs (upper) and channel-rich RuCu NSs (lower); (b) the PDOS of H_2O adsorption on RuCu NSs; (c) the site-dependent PDOS of Ru 4d bands; (d) the site-dependent PDOS of Cu 3d bands. Adapted with permission from ref. 151. Copyright 2019, Wiley-VCH Verlag GmbH &Co. KGaA, Weinheim.

and $H_{ads} + H_{ads} \rightarrow H_2$ (Tafel step). The reaction path can be easily determined from the experimentally calculated Tafel slope.

Advanced HER catalysts generally contain three indicators: higher catalytic efficiency, longer durability, and lower overpotential. Chen and coworkers indicated that the 3D interconnected structure of Pt-SSs@PEI ensured long-term stability of the HER.[184] Huang and coworkers synthesized RuCu NSs with channel-rich structures composed of crystallized Ru and amorphous Cu, showing attractive low overpotentials and small Tafel slopes.[151] DFT calculations revealed that the channel-rich structures caused lattice distortion near the channel region, which is favorable for the surface electronic activation of RuCu NSs (Fig. 11). The induced short-range disorder near the channel region will minimize the intermediating energetic cost of bond-dissociation with lattice relaxation. Therefore, the highly branched structure is conducive to improving HER catalytic performance and is a strong competitor for future commercial development.

A number of noble metal nanodendritic electrocatalysts with excellent performance have been identified in recently reported studies, including monometallic, bi-/tri-metallic, supported and core–shelled electrocatalysts. HER performance is mainly evaluated by testing the overpotential (typically at 10 mA cm^{-2}) and Tafel slope. The smaller the overpotential, the lower the voltage required for the reaction and the higher the reactivity of the catalyst; the smaller the Tafel slope, the higher the charge transfer capability of the catalyst. Although the performance of electrocatalysts is governed by the synthetic method, it is certain that monometallics tend to exhibit slightly inferior performance to the "modified" electrocatalysts, *e.g.*, the overpotential and Tafel slope of Pd[185] are larger than those of $Pd_{43}Ag_{21}Pt_3$[149] and AuPtPd,[188] *etc.* Moreover, because the HER occurs under alkaline conditions with an additional water dissociation step, the same electrocatalyst performs better under acidic conditions than under alkaline conditions, such as PtRh.[186] A more detailed comparison of the HER catalytic activity of dendritic noble metals and noble metal alloys reported in recent years is shown in Table 1.

Table 1 Summarization of electrochemical HER performance of noble metal nanodendrites

Materials	Tafel slope (mV dec^{-1})	Overpotential (mV) at 10 mA cm^{-2}	Electrolyte	Ref.
Pd	49	83	0.5 M H_2SO_4	185
PtRh	40	27	0.5 M H_2SO_4	186
AuPt	34	50	0.5 M H_2SO_4	187
$Pd_{43}Ag_{21}Pt_3$	19.6	9	0.5 M H_2SO_4	149
AuPtPd	36	29	0.5 M H_2SO_4	188
PtNi/Pt	23	21	0.5 M H_2SO_4	189
O–Pt on Au	31	18	0.5 M H_2SO_4	190
$Pt_{77}Pd_{23}$/rGO	36	57	0.5 M H_2SO_4	191
Au@Rh_3Cu	33.4	83	0.5 M H_2SO_4	192
Pt@PEI	28	64.6	0.5 M H_2SO_4	184
Rh_2Ir	17.3	12	0.1 M $HClO_4$	193
IrW/C	12	—[a]	0.1 M $HClO_4$	157
Pd_{45}@Ir_{55}	26	11	0.1 M $HClO_4$	158
$Pt_{56}Rh_{44}$	63.3	20	0.5 M KOH	194
Ru	49	43.4	1 M KOH	195
PtRh	47	28	1 M KOH	186
Rh_2Ir	25.9	9	1 M KOH	193
PdH	130	358	1 M KOH	156
RuCu/C−250 °C	15.3	20	1 M KOH	151
IrW/C	20	—	1 M KOH	157
Pd@RhPd	53	49	1 M KOH	196

[a] Not mentioned.

HER is a cathodic reaction for hydrogen production by electrolysis of water, which usually uses Pt as a commercial electrocatalyst in an acidic medium, so it brings higher commercial cost, which is the most important problem limiting its commercialization. Moreover, the acidic electrolyte will corrode the electrolyzer, which brings safety problems. In contrast, the HER in an alkaline medium can relatively avoid this problem. However, the slow reaction kinetics of the alkaline HER still restricts its practical applications. The current research strategy is focused on finding alkaline HER electrocatalysts with high catalytic activity.

4.1.2 Oxygen reduction reaction (ORR). The pathway followed by most noble metals is the complete reduction of O_2 to H_2O, *i.e.*, 4-electron ORR (in acidic media: $O_2 + 4H^+ + 4e^- \rightarrow 2H_2O$; in alkaline media: $O_2 + 2H_2O + 4e^- \rightarrow 4OH^-$). The contribution of nanodendrites to the ORR is attributed to the large number of high-index crystal facets exposed at the edge of the structure since the ORR activity is particularly facet-dependent.[197,198] This crystallographic dependence appears probably due to the structural sensitivity of the OH_{ads} species

to Pt{*hkl*}, which can selectively block the active site of O_2 adsorption on different crystal facets, thus retarding the ORR kinetics.[55] Chen and coworkers synthesized FePt nanodendrites with a single crystal structure and high-index {311} facet terminated, which showed stronger ORR catalytic activity compared to FePt nanospheres with {111} facets, nanocubes with {200} facets, and Pt nanocrystals.[199] The results indicated that the high-index exposed facet of highly branched nanodendrites is the key feature to enhance the ORR electrocatalytic activity, which could be attributed to the favorable adsorption of O_2 molecules on the stepped surfaces. Of course, not only the facet-dependent effect but also the strain effect, defect effect, and ligand effect play important roles in affecting the performance of the ORR. Xia and coworkers proposed Pd–Pt bimetallic nanodendrites in 2009.[55] The ORR measurements indicated that Pd–Pt bimetallic nanodendrites had the lowest initial and half-wave potential, and the mass activity of the Pd–Pt nanodendrites was 0.204 mA mg_{Pd+Pt}^{-1} at 0.9 V, which is 2.1 and 4.3 times greater than that of the Pt/C and Pt black at room temperature (Fig. 12a–d). Lin and coworkers synthesized PdCuPt ternary nanodendrites with low Pt-content and indicated the enhanced electrocatalytic performance of the ORR in an acidic solution compared with the commercial Pt/C (Fig. 12e–h).[200] The mass activity of the PdCuPt nanodendrites was 1.73 A mg_{Pt}^{-1} at 0.85 V *vs.* RHE, and PdCuPt nanodendrites exhibited a positive onset (0.933 V) and half-wave ($E_{1/2}$) (0.864 V) potentials (Fig. 12f). Moreover, after the 5k cycles stability test, there was still 70% electrochemical surface area maintained (Fig. 12h).

It is well known that the dissolution of metal components is one of the main reasons for the degradation of Pt-based electrocatalysts, and it has not been completely improved in engineering aspects. However, the rational use of instability under electrochemical conditions can also bring positive effects. For example, Yi and coworkers prepared hollow PdPt nanocages by applying potential cycling treatment on core–shell Pd@Pt nanodendrites, which maintained high structural stability after long-term durability testing.[201] Sun and coworkers reported an ultra-stable PtRh ND electrocatalyst and explored the reasons for the stability enhancement.[202] First, they found that $E_{1/2}$ of PtRh NDs/C remained almost unchanged and the mass activity of PtRh NDs/C dropped by about only 12% from 10k to 100k ADT cycles (Fig. 13a and b). This is undoubtedly one of the most stable nanocatalysts in the ORR. They dug into the reason deeply. As shown in Fig. 13c, the CV curves of PtRh NDs/C changed significantly after 10k ADT cycles, which include the location and number of peaks in the hydrogen region, indicating that the microstructure evolution of the nanocatalysts surface may occur during this period. TEM characterization and DFT calculation showed that due to the difference in dissolution energy between Pt and Rh atoms, a Pt-rich shell was formed on the surface after 100k ADT cycles. It is the structural evolution that enhances the dissolution resistance and improves the stability of the PtRh NDs (Fig. 13d–g).

ORR electrocatalysts are evaluated mainly by $E_{1/2}$ and the current density at 0.9 V. The closer the $E_{1/2}$ value is to 1.23 V, the better the electrocatalytic performance. In addition, electrochemical active surface areas (ECSAs) reflect the exposure of active sites on the surface of the electrocatalyst, which can be used to initially judge the activity of the electrocatalyst on the one hand, and to calculate the intrinsic activity of the electrocatalyst based on the value of ECSAs on the other hand. Among the ORR nanodendritic electrocatalysts reported in recent years, some of them exhibit excellent electrocatalytic activity (Table 2). For example, Pt–Co reported by Shen and coworkers exhibited the

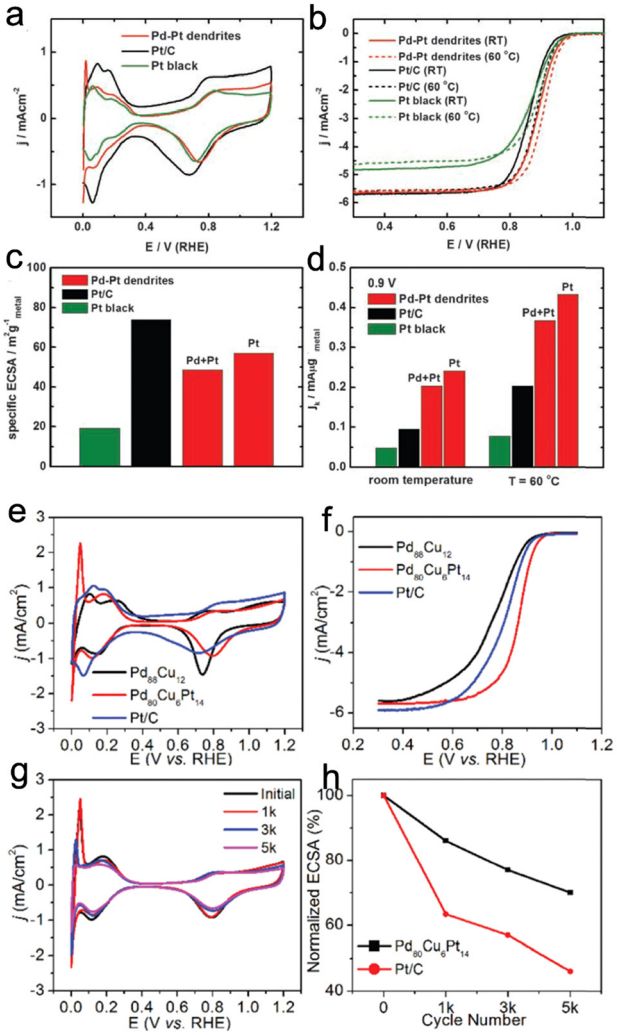

Fig. 12 (a) CV curves recorded at room temperature in an Ar-purged 0.1 M $HClO_4$ solution with a sweep rate of 50 mV s^{-1}; (b) ORR polarization curves for the Pd–Pt nanodendrites, Pt/C catalyst, and Pt black recorded at room temperature and 60 °C in an O_2-saturated 0.1 M $HClO_4$ solution with a sweep rate of 10 mV s^{-1} and a rotation rate of 1600 rpm; (c) specific ECSAs for the Pd–Pt nanodendrites, Pt/C catalyst, and Pt black. (d) Mass activity at 0.9 V *versus* RHE for these three catalysts. Mass activities were given as kinetic current densities (j_k) normalized in reference to the loading amount and ECSA of metal, respectively. Adapted with permission from ref. 55. Copyright 2009, Science; (e) CV curves of PdCu, PdCuPt NDs and commercial Pt/C catalysts in N_2-saturated 0.1 M $HClO_4$ solution at a sweep rate of 50 mV s^{-1}; (f) ORR polarization curves; (g) CV curves of $Pd_{80}Cu_6Pt_{14}$ NDs and (h) loss of ECSA for $Pd_{80}Cu_6Pt_{14}$ NDs and Pt/C during the stability test. Adapted with permission from ref. 200. Copyright 2017, The Royal Society of Chemistry.

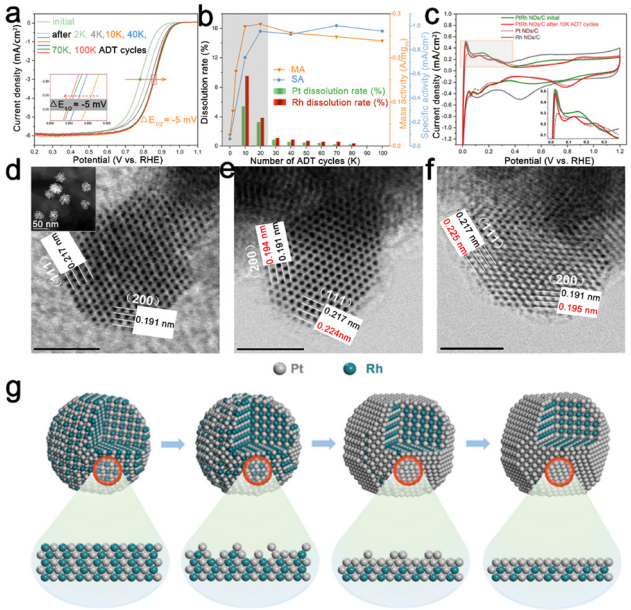

Fig. 13 (a) Positive-going LSV curves and its partial enlargement (inset) at orange rectangle for PtRh NDs/C; (b) MA and SA of PtRh NDs/C and dissolution rate of Pt and Rh; (c) CV curves of PtRh NDs/C before and after the first 10k ADT cycles, Pt NDs/C, and Rh NDs/C and their partial enlargement (inset) in the orange rectangle; (d–f) HR-STEM images of PtRh NDs at 0k, 10k, and 100k ADT cycles, respectively (scale bar: 2 nm) (inset: HAADF-STEM image); (g) schematic illustrations of the structure of the end of PtRh NDs during the 10k ADT cycles. Adapted with permission from ref. 202. Copyright 2022, American Chemical Society.

maximum $E_{1/2}$ with a value of 0.95 V.[161] $PtCu_3$@Pt_3Cu@Pt reported by Chen and coworkers exhibited the best current density with a value of 1.55 A mg^{-1}.[203] Unfortunately, the work reported so far only stays at the stage of interpreting the catalytic performance of the ORR with experimental data, but the electrocatalytic performance is more affected by the electronic structure. What are the changes in the electronic effect brought by the highly branched structure? and the effect on the intrinsic catalytic activity of the ORR is still unknown.

ORR is commonly used as the positive electrode in hydrogen–oxygen fuel cells and methanol fuel cells, and similarly, commercial Pt catalysts are still subject to high cost and low activity. The ORR not only has slow reaction kinetics, but also suffers from incomplete reduction and even poisoning by diffusers from the negative electrode in fuel cell devices. Therefore, to solve the problems of catalyst cost, activity and stability, recent research hotspots have focused on interface engineering, strain engineering and single-atom engineering.

4.1.3 Methanol oxidation reaction (MOR). The MOR is a sluggish reaction because it is a $6e^-$ involved reaction pathway (under alkaline conditions: $CH_3OH + 6OH^- \rightarrow CO_2 + 5H_2O + 6e^-$). The most widely accepted mechanism is the dual-pathway mechanism proposed by Khazova.[204] According to this mechanism, methanol oxidation results in the formation of various intermediates (CO, HCHO and HCOOH) on the catalyst surface, while CO_{ads} poisons the surface of noble metals and prevents further reactions. The introduction of oxyphilic metals and heteroatoms with electron affinity are common ways to improve toxicity resistance.[205] It has also been suggested that the MOR pathways are different on different crystal facets.[207] For the {111} and {110} facets, the MOR reaction follows a parallel non-CO pathway in a high potential range, while on the {100} facet, the reaction follows a CO formation pathway over a wide potential range. Therefore, reasonable design of the surface structure of the nanodendrites can improve the CO toxicity resistance. The activity of the nanomaterials can be preliminarily determined by comparing the value of ECSAs, which has a positive correlation with mass activity. For example, Shen and coworkers designed hollow Pt–Ni–Co nanodendrites by selectively etching the Ni rich core.[208] The structure features highly branched and hollow characteristics, resulting in the highest ECSA values compared to solid Pt–Ni–Co NDs and Pt/C. Therefore, hollow Pt–Ni–Co NDs possessed the best MOR performance.

We designed a series of nanodendrites in the previous work, including PtRu alloys with variable proportions, controllable structures, and replaceable second metals.[150] Specific proportions of 2D PtRu nanodendrites exhibited the highest ECSAs, CO toxic resistance and stability (Fig. 14a–c). The synergistic electronic and structural effects in 2D highly branched PtRu nanodendrites result in enhanced MOR performance. Wang and coworkers synthesized PtRuNi nanoframes surrounded by ultrathin Ru nanodendrites (PtRuNi FDs), and the higher MOR activity was attributed to the unique 3D open architecture and suitable composition. In acidic electrolyte, PtRuNi FDs can reach the mass activity of 1.49 A mg_{Pt}^{-1} for the MOR, which is 2.9-fold higher than that of commercial Pt/C, and also show impressive catalytic durability (Fig. 14d–g).[206]

Table 3 summarizes the nanodendritic catalysts reported in recent years, and it can be found that all of these nanodendrites exhibit excellent MOR performance. Table 3 lists several parameters: mass activity, specific activity, ECSA values and type of electrolyte, where the electrolyte for alcohol oxidation is a mixture of A and B. A is KOH or H_2SO_4 and B is the alcohol reactant. Summarizing the contents in the table, it can be found that the mass activity in alkaline electrolytes is much higher than that in acidic solutions because it is easier to form surface OH_{ads} in alkaline solutions. Surface toxic intermediates CO_{ads} can be easily consumed by OH_{ads}, and thus higher activity is obtained. In addition, Au@Pt/MoS_2-2 reported by Wang and coworkers exhibited the best mass activity,[246] and PtRu reported by bao and coworkers exhibited the best specific activity.[150]

MOR is used as the negative reaction of a methanol fuel cell, and its positive reaction is the ORR. It was mentioned in the last section that the commercialization process of the ORR is affected by the diffusion of substances from the negative electrode, which is due to the severe permeation of methanol at the proton exchange membrane, resulting in the reduced utilization of methanol fuel. The main factors limiting the commercial application of MOR are cost issues on the one hand and activity and stability issues on the other. Methanol has a slow reaction rate at low temperatures, which directly

Table 2 Summarization of electrochemical ORR performance of noble metal nanodendrites

Materials	$E_{1/2}$ (V)	Mass activity at 0.9 V (A mg^{-1})	ECSA (m^2 g^{-1})	Electrolyte	Ref.
Pt	0.912	0.1712	44.0	0.1 M $HClO_4$	82
Pt	—[a]	0.1429	43.4 ± 0.2	0.1 M $HClO_4$	105
Pt	0.86	—	117.47	0.1 M $HClO_4$	209
Pt–Pd	~0.8	—	18.56	0.1 M $HClO_4$	86
$Pt_{79}Co_{21}$	—	0.12829 (at 0.75 V)	29.79	0.1 M $HClO_4$	85
Pt–Co	0.95	—	35.6	0.1 M $HClO_4$	161
PtCo	0.60	—	64.28	0.1 M $HClO_4$	210
$Au_{75}Pt_{25}$	—	—	79.48	0.1 M $HClO_4$	211
AuPt	0.87	0.03155	29.67	0.1 M $HClO_4$	187
Pt–Ni	—	1.51 (at 0.93 V)	73.4	0.1 M $HClO_4$	212
$Pt_{55}Cu_{45}$	0.891	0.816	63.19	0.1 M $HClO_4$	213
$Pt_{78}Cu_{22}$	—	0.32	50.78	0.1 M $HClO_4$	214
Cu–Pd	0.818	—	36.2	0.1 M $HClO_4$	215
Pd–Cu	—	—	80.2	0.1 M $HClO_4$	216
PtCu–N	0.927	1.23	106.5	0.1 M $HClO_4$	217
PdCuPt	0.864	—	84	0.1 M $HClO_4$	200
Pt/C	—	0.37	68.5	0.1 M $HClO_4$	218
Pt_1Pd_1/C	0.916	0.85	53.8	0.1 M $HClO_4$	219
Pt–Ni/C	0.873	0.64	51.7	0.1 M $HClO_4$	220
Au/Pt_3Ni	0.892	0.479	—	0.1 M $HClO_4$	221
Au–Pd–Pt/rGO	—	0.145	44.37	0.1 M $HClO_4$	163
PtDs/gdsDNA/rGO	0.9	0.401	67.2	0.1 M $HClO_4$	222
Pt@Au′/C	0.93	0.56	65	0.1 M $HClO_4$	223
$PtCu_3$@Pt_3Cu@Pt	0.93	1.55	80.1	0.1 M $HClO_4$	203
AuNi	0.911	0.09 (at 0.85 V)	—	0.5 M H_2SO_4	224
PtPdRu	0.611	—	96.8	0.5 M H_2SO_4	225
Pt/C	0.903	0.109	45	0.5 M H_2SO_4	123
PdPt/C	—	02309 (at 0.85 V)	27.5	0.5 M H_2SO_4	201
Pd/C	0.851	—	17.21	0.1 M KOH	226
$PdH_{0.33}$/C	0.911	0.719 ± 0.013	57.4	0.1 M KOH	227
$Rh_{20}Pd_{80}$/C	—	0.48 (at 0.8 V)	22	0.1 M KOH	228
AuPtPd	0.924	0.05849 (at 0.8 V)	27.65	0.5 M KOH	188

[a] Not mentioned.

limits its commercial application. In addition, CO can easily coordinate with the d-orbital of Pt, causing catalyst poisoning and reducing stability. Therefore, the current research direction is mainly focused on finding electrocatalysts with high activity and high anti-toxicity ability.

4.1.4 Ethanol oxidation reaction (EOR). Ethanol is an eco-friendly and renewable fuel that can be obtained from biomass, the products of which are CO_2 and H_2O after complete oxidation. In recent years, many efficient EOR nanodendrites catalysts have been reported, as listed in Table 4, they all show good activity and stability, which can be used as an important reference for subsequent catalysts design. It can be found that EOR often uses alkaline electrolytes. This is because the alcohol oxidation reaction adopts a reaction path of gradual proton detachment and reacts with OH^- in solution to produce H_2O, which can accelerate the reaction kinetics. For example, the ternary alloy reported by Wang and coworkers exhibited the highest mass activity and specific activity among the nanodendrite species with 16.32 A mg^{-1} and 81.64 mA cm^{-2}, respectively.[159]

The complete oxidation product of ethanol is CO_2 ($CH_3CH_2OH + 12OH^- \rightarrow 2CO_2 + 9H_2O + 12e^-$), a pathway involving $12e^-$ with multiple intermediates. However, most of the electrocatalysts catalyze ethanol into CH_3COOH ($CH_3CH_2OH + 5OH^- \rightarrow CH_3COO^- + 4H_2O + 4e^-$), which not only wastes energy but also generates acetate on the positive electrode, limiting the sustainability of ethanol fuel cells. The subsequent work should also explore the method for high-performance EOR catalysts under acidic conditions.

The core problem of the EOR is the splitting of C–C bonds. The CO_2 conversion rate can be preliminarily determined by the high ratio of the forward peak current density to the backward one (j_f/j_b).[252] Recently, only a few studies have realized efficient C–C bond splitting with relatively low activity.[253–256] There is evidence that the presence of high-index facets can promote the breaking of the C–C bond.[257]

The dendritic structure of the nanocatalysts not only exposes more active sites but also enables controlled exposure of crystal planes with adjustable composition, which will open a new gate for promoting the complete oxidation of the EOR.

4.1.5 Formic acid oxidation reaction (FAOR). Formic acid is considered as a promising fuel due to its high energy density of 1740 W h kg^{-1} or 2086 W h L^{-1}, less toxicity and lower crossover flux.[258] It is widely believed that the electrocatalytic oxidation of HCOOH proceeds by a dual path mechanism: the direct reaction pathway ($HCOOH \rightarrow COOH_{ads}/HCOO_{ads} + H^+ + e^- \rightarrow CO_2 + 2H^+ + 2e^-$) (Fig. 15a–c) and the indirect reaction pathway ($HCOOH \rightarrow CO_{ads} + H_2O \rightarrow CO_2 + 2H^+ + 2e^-$).[259]

The difference in intermediates can be reflected in the CV curves, and the reaction path can be initially determined based on the difference between the initial and peak potentials, as reported by Chen and coworkers. They prepared PtAu

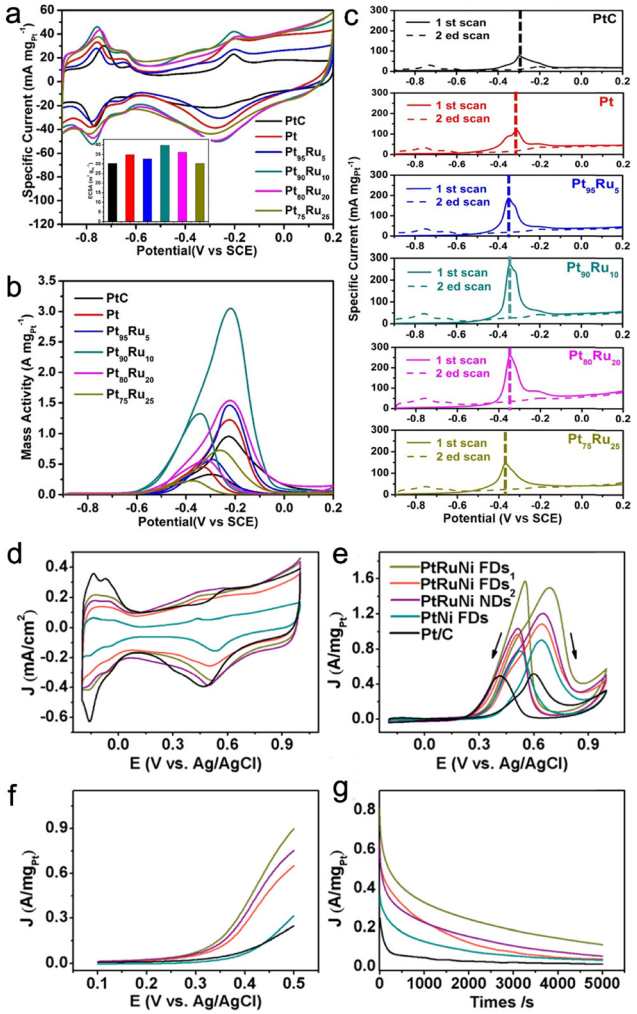

Fig. 14 (a) CV curves of Pt, $Pt_{95}Ru_5$, $Pt_{90}Ru_{10}$, $Pt_{80}Ru_{20}$, $Pt_{75}Ru_{25}$ NDs, and commercial PtC collected in 1.0 M KOH (inset: calculated ECSAs) and (b) in 1.0 M KOH and 1.0 M methanol; (c) CO stripping voltammograms collected in 1.0 M KOH at a scan rate of 50 mV s^{-1}. Adapted with permission from ref. 150. Copyright 2019, The Royal Society of Chemistry; (d) CV curves of different catalysts in N_2-saturated 0.1 M $HClO_4$ solution; (e) CV curves, (f) enlarged CV curves in the forward scanning regions, and (g) long term *i*–*t* curves of different catalysts in 0.1 M $HClO_4$ and 0.5 M methanol solution. Adapted with permission from ref. 206. Copyright 2019, The Royal Society of Chemistry.

nanodendrites as FAOR catalysts and compared the cyclic voltammogram (CV) curves with Pt NPs.[260] The PtAu nanodendrites have a low onset potential (0.20 V) and the current density is significantly enhanced in the low potential region (0.05–0.45 V), indicating that the oxidation of formic acid on the alloyed proceeds mainly through the preferred dehydrogenation path. As for Pt NPs, the onset potential is 0.03 V and the peak potential is 0.62 V, indicating that the oxidation of formic acid proceeds mainly through the dehydration pathway with intermediate CO_{ads} involved. PtAu nanodendrites exhibit excellent stability due to the elimination of CO_{ads} poisoning during the oxidation process.

Sun and coworkers utilized *in situ* Fourier transform infrared spectroscopy (*in situ* FTIR) to explore the process of formic electrooxidation of PtPb single-crystalline nanodendrites (PtPb SND), Pt/C-JM and Pd black in the molecular level (Fig. 15c–e).[261] Three negative-going peaks at 1214, 1400 and 1720 cm^{-1} are the characteristic peaks of HCOOH. The positive-going band at 2343 cm^{-1} is considered to be the asymmetric stretching vibration of CO_2. The bipolar peak at around 2030 cm^{-1} is attributed to linear bound CO (CO_L), *i.e.*, a toxic intermediate produced from the indirect pathway. Clearly, no CO_L peaks are observed on PtPb SND and Pd black compared to Pt/C-JM even at relatively low potentials, demonstrating the direct reaction path. Moreover, compared to Pd black, PtPb SND exhibited higher activity and stability. They attributed the greatly enhanced activity of PtPb SND to the porous and highly branched structure, which provides more active sites.

Formic acid is considered to be a safer fuel than methanol, and its membrane penetration is lower than that of methanol, which solves the problem of fuel diffusion to the positive electrode to some extent. Pt and Pd catalysts are still mainly used as electrocatalysts. It has been evidenced that Pd is more suitable for formic acid fuel cell catalysts because formic acid proceeds on its surface mainly through the direct oxidation pathway. Despite numerous strategies designed to avoid the occurrence of the indirect reaction pathway, in practice, formic acid oxidation catalysts still suffer from rapid deactivation in electrolyte solutions. Therefore, the research on the FAOR mechanism in the field of nanodendrites should be continued.

4.1.6 CO_2 reduction reaction (CO_2RR). Cu-based catalysts can promote the C–C coupling reaction, and thus their electrocatalytic CO_2RR products include high energy density multicarbon alcohols or hydrocarbons (C_2 or C_{2+}), making them the most studied CO_2 electroreduction catalysts at present. Sun and coworkers reported that nanodendrites structure can improve the electrocatalytic performance of Cu catalysts, especially the formation of multicarbon products. The fractal Cu dendritic structure has high ECSAs and forms an abundant conductive network that facilitates electron and mass transfer, leading to superior kinetics for the formation of multi-carbon products by CO_2 electroreduction. The results showed that the yield of ethylene and C_3 (*n*-PrOH and propanal) on Cu nanodendrites are increased by 70–120% and 60–220%, respectively, compared to the initial Cu particles.[262]

Cu-based noble metal alloy materials have also been explored. Li and coworkers designed the Pd–Cu alloy nanodendrites with dual properties of alloying and branching structure, large surface area and abundant uncoordinated sites which are ideal for electrochemical catalysts (Fig. 16a–e).[263] In 0.1 M $KHCO_3$ solution, CO_2RR product analysis indicated that formate was the predominant reduction product in the catholyte ($CO_2 + 2e^- + H^+ \rightarrow HCOO^-$). The formate faradaic efficiency of nd-PdCu-1 was measured to be ~82% at 0 V and >90% between −0.1 V and −0.4 V. Pd–Cu NDs still showed remarkable stability and selectivity at −0.4 V (Fig. 16f–j). Computational simulations evidenced that Cu atoms weakened the adsorption of *CO and stabilized the adsorption of *OCHO on adjacent Pd atoms, so the selectivity of formic acid was improved.

Table 3 Summarization of electrochemical MOR performance of noble metal nanodendrites

Materials	Mass activity (A mg^{-1})	Specific activity (mA cm^{-2})	ECSA (m^2 g^{-1})	Electrolyte A	Electrolyte B	Ref.
Pt/Au	0.185	—	46.41	0.5 M H_2SO_4	0.5 M methanol	229
Pt_1Cu_1	1.4	3.01	46.5	0.5 M H_2SO_4	0.5 M methanol	230
Pt	—[a]	~27	43.4 ± 0.2	0.5 M H_2SO_4	1 M methanol	105
PtRu	1.08	2.7	47.7	0.5 M H_2SO_4	1 M methanol	63
PtRu	0.5632	21.5	66.7	0.5 M H_2SO_4	1 M methanol	150
PtRu-a	—	1.62	18.9	0.5 M H_2SO_4	1 M methanol	231
Pt_3Pd_1	—	1.36	9.68	0.5 M H_2SO_4	1 M methanol	232
$Ni_{0.20}Pt_{0.80}$	2.2	—	53.0	0.5 M H_2SO_4	1 M methanol	116
PtNiRu	0.683	1.97	34.7	0.5 M H_2SO_4	1 M methanol	233
PtPdCu	0.688	1.154	59.6	0.5 M H_2SO_4	1 M methanol	234
PtRuFe	1.14	2.03	56.4	0.5 M H_2SO_4	1 M methanol	235
Pt/PHCS	0.305	—	51.6	0.5 M H_2SO_4	1 M methanol	236
TP-BNGN	0.6472	—	81.6	0.5 M H_2SO_4	1 M methanol	237
G@(PEI/Au)3.5@Pt	0.365	0.363	100.8	0.5 M H_2SO_4	1 M methanol	238
CS Au–Pt	0.45	1.28	35.2	0.5 M H_2SO_4	1 M methanol	239
PtPdAg	1.58	3.75	42.02	0.1 M $HClO_4$	0.2 M methanol	240
Pt_3Cu	—[a]	0.50	112.5	0.1 M $HClO_4$	0.5 M methanol	33
PtRu	1.14	2.66	42.21	0.1 M $HClO_4$	0.5 M methanol	68
PtRuNi	1.49	—	47.4	0.1 M $HClO_4$	0.5 M methanol	206
Pt–Ni/C	~2.5	~5.5	51.7	0.1 M $HClO_4$	0.5 M methanol	220
$Pt_{79}Co_{21}$	0.66623	2.51	29.79	0.1 M $HClO_4$	1 M methanol	85
$Pt_{47}Rh_8Cu_{45}$/C	0.38	1.22	31.9	0.1 M $HClO_4$	1 M methanol	241
RG-Pd	—	0.5098	—	0.1 M KOH	1 M methanol	242
AuPt ANDs/rGO	0.686	1.95	64.8	0.5 M KOH	0.5 M methanol	243
PtCu–O	4.43	—	29.3	0.5 M KOH	1 M methanol	244
Pd@RhPd	—	3.373	15	1 M KOH	0.5 M methanol	196
PtRu	3.06	123	39.4	1 M KOH	1 M methanol	150
Pt–Pd	—	~120	92.0	1 M KOH	1 M methanol	245
PdPtCu	2.67	—	46.3	1 M KOH	1 M methanol	78
$Pd_{43}Ag_{21}Pt_{36}$	~1.9	2.9	64.5	1 M KOH	1 M methanol	149
Au@Pt/MoS_2-2	6.24	—	—	0.5 M NaOH	1 M methanol	246

[a] Not mentioned.

Table 4 Summarization of electrochemical EOR performance of noble metal nanodendrites

Materials	Mass activity (A mg^{-1})	Specific activity (mA cm^{-2})	ECSA (m^2 g^{-1})	Electrolyte A	Electrolyte B	Ref.
PdP	3.22	—[a]	34.2	1 M KOH	1 M ethanol	77
PdAg	2.6	—	69.5	1 M KOH	1 M ethanol	92
Pt1Rh1	0.4621	—	64.1	1 M KOH	1 M ethanol	247
Pt_2Fe	3.6925	7.02	52.6	1 M KOH	1 M ethanol	248
PdPtCu	3.79	—	46.3	1 M KOH	1 M ethanol	78
PtPdRu	16.32	81.64	68.74	1 M KOH	1 M ethanol	159
PtPdCu	5.59	15.82	35.3	1 M KOH	1 M ethanol	249
Pd_7/Ru_1	1.15	—	15.877	1 M KOH	1 M ethanol	250
Au@Pd	1.746	—	228.72	1 M KOH	1 M ethanol	251
CPT Rh	0.1853	0.36	—	1 M NaOH	1 M ethanol	70
$Pd_{43}Ag_{21}Pt_{36}$	3.33	5.16	64.5	1 M NaOH	1 M ethanol	149

[a] Not mentioned.

Li and coworkers proposed Bi–Pd single atom alloy (SAA) NDs with Bi atomically dispersed in Pd nanodendrites as efficient CO_2 reduction electrocatalysts.[264] The doping of Bi reduced the H coverage and decreased free energy of *COOH generation, so it is beneficial to reduce CO_2 to CO at low overpotential ($CO_2 + 2e^- + 2H^+ \rightarrow CO + H_2O$). The Bi_6Pd_{94}-SAA ND catalyst achieved faradaic efficiencies (FEs) of 90.5% and 91.8% for CO over at overpotentials of only 290 and 200 mV in H-type and gas diffusion flow cells.

The reduction of CO_2 to polycarbonate products is of great importance in the energy field. However, this topic is still at the stage of fundamental experiments, and the main problem is the electrocatalysts. First, competitive HER are inevitable at lower potentials, and second, only a few electrocatalysts are currently available for the synthesis of multi-carbon products, and the poor selectivity of existing catalysts makes the practical application of CO_2RR still a long way off. In the future, it will be significant scientific research work if we can find suitable catalysts to achieve 100% efficiency of CO_2RR to produce methanol or ethanol, which can be connected with methanol or ethanol fuel cells to combine into a closed carbon cycle.

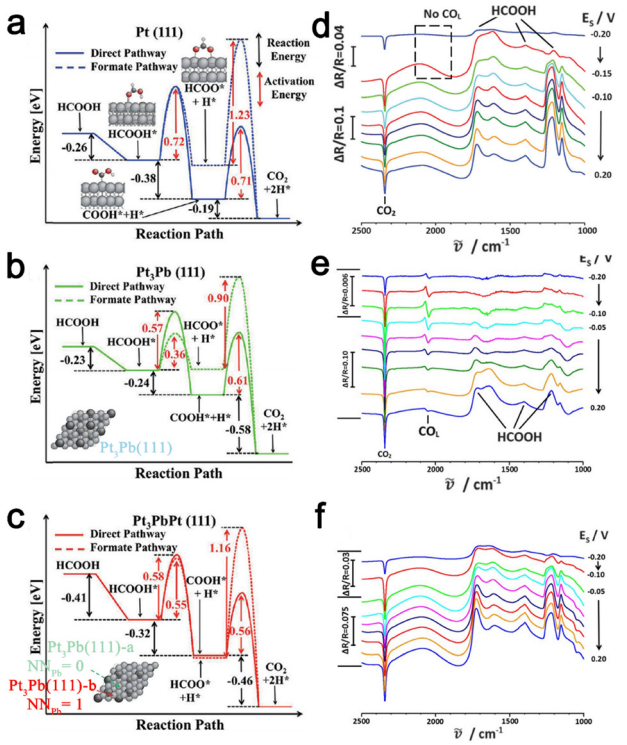

Fig. 15 (a–c) Reaction pathways of HCOOH → CO_2 + 2H* with reaction/activation energies of elementary steps on different model surfaces. Here, the final product H* is located at the most stable adsorption site on the corresponding surface; thus three surfaces have different total reaction energies because of different H adsorption strengths (inset: (b) surface models of $Pt_3Pb(111)$, and (c) $Pt_3PbPt(111)$ atoms. Gray (black) stands for Pt(Pb) atoms). Adapted with permission from ref. 259. Copyright 2012, American Chemical Society; *in situ* FTIR spectra of HCOOH oxidation on (d) PtPb SND, (e) Pt/C-JM and (f) Pd black at different potentials. E_S was varied from −0.20 to 0.20 V, E_R = −0.25 V *vs.* SCE. Adapted with permission from ref. 261. Copyright 2016, The Royal Society of Chemistry.

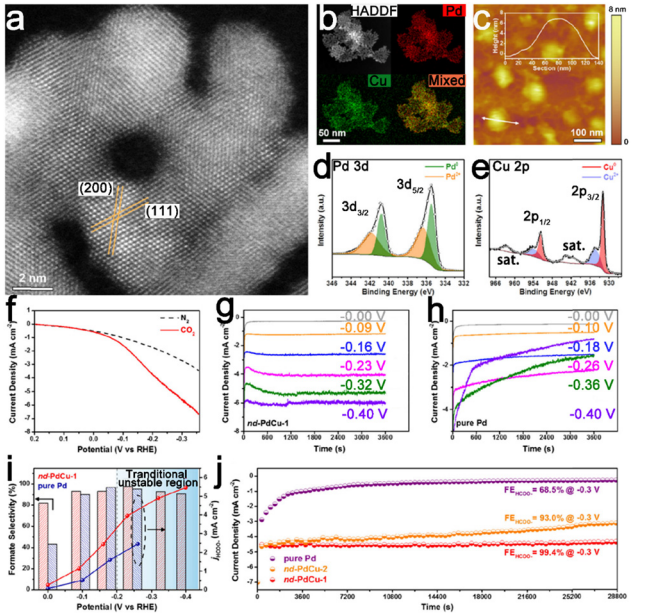

Fig. 16 (a) HAADF-STEM images and (b) EDS elemental mapping of nd-PdCu-1; (c) AFM image of nd-PdCu-1, inset shows the height profile across a nanodendrite; (d) Pd 3d XPS and (e) Cu 2p XPS spectra of nd-PdCu-1; CO_2RR performance of nd-PdCu-1 in 0.1 M $KHCO_3$. (f) Polarization curves of nd-PdCu-1 in CO_2- or N_2-saturated electrolyte; (g and h) chronoamperometric curves of nd-PdCu-1 and pure Pd at different working potentials; (i) calculated formate faradaic efficiency and partial current density of nd-PdCu-1 and pure Pd at different working potentials; (j) long-term chronoamperometric stability of pure Pd, nd-PdCu1 and nd-PdCu-2 at −0.3 V for 8 h. Adapted with permission from ref. 263. Copyright 2021, American Chemical Society.

4.2 Others applications

4.2.1 Biosensing. Nanodendrites have a large number of nano gaps, and the tips and edges can serve as the hot spots for large electromagnetic field enhancement, which can absorb a large number of molecules to be measured and generate strong surface-enhanced Raman scattering (SERS) signals.[265–269] The sharper tips and the increased number of tips can produce higher electromagnetic fields concentrations compared to spherical particles, so nanodendrites have promising applications in SERS. Due to the surface plasmon resonance (SPR) properties of Ag and Au nanomaterials, they show remarkable optical properties in the visible range, making them widely used in the field of SERS detection.

Xu and coworkers synthesized highly branched, concave Au/Pd bimetallic NCs with strong SERS signals for crystal violet at a very low concentration of 10^{-12} M[270] (Fig. 17a). In their work, the SERS enhancement factors (EFs) were estimated to be 1.12×10^7. Yang and coworkers synthesized Ag NDs, and they showed superior SERS sensitivity using rhodamine 6G as a probe molecule, with a detection concentration as low as 5×10^{-16} M.[271] And Ag NDs reported in this work broke the

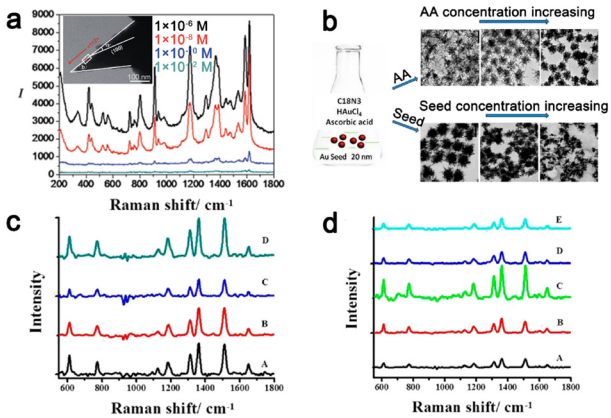

Fig. 17 (a) SERS spectra of crystal violet adsorbed on the concave branched Au/Pd bimetallic nanocrystals. The SERS spectra were obtained with λ_{ex} = 514 nm excitation, P_{laser} = 1 mW, and t = 20 s (inset: TEM image of one branch of an Au/Pd nanostar). Adapted with permission from ref. 270. Copyright 2013, Wiley-VCH Verlag GmbH & Co. KGaA, Weinheim; (b) schematic illustration of the influence of AA and Au seed concentration on the formation and morphology of gold nanodendrites; SERS signals obtained from R6G molecules on gold nanodendrites; (c) gold nanodendrites obtained using varying volumes of seed: A, 0.05 mL; B, 0.2 mL; C, 0.5 mL; D, 1 mL; (d) gold nanodendrites obtained using varying volumes of AA: A, 2 μL; B, 5 μL; C, 7 μL; D, 10 μL; E, 14 μL. Adapted with permission from ref. 272. Copyright 2013, American Chemical Society.

theoretical limit of electromagnetic enhancement with an ultra-high factor of 10^{13}. Camargo and coworkers prepared hollow Ag–Au nanodendrites as efficient SERS substrates for the detection of 4-mercaptopyridine (4-MPy) and rhodamine 6G (R6G) with detection limit concentrations of 5×10^{-7} and 5×10^{-6} mol L^{-1}, respectively.[273] The performance enhancement derives from the structure characteristics, such as hollow interiors, the sharp tips/branches on the surface, and its higher surface-to-volume ratios than their solid and/or rounded counterparts. Wang and coworkers report that the hierarchical structure and large surface area of Ag nanodendrites can be applied as a unique substrate for SERS detection of pyridine molecules.[274] Furthermore, Opallo and coworkers obtained Pd nanodendrites and found their application in the prostate specific antigen (PSA) SERS biosensor with the detection limit of 10 ng mL^{-1}.[275] Karnthaler and coworkers developed Ag nanodendrites for SERS with long-term stability even after one year, which facilitates practical applications.[276]

Moreover, this high sensitivity is also related to the number of nanodendrite branches. Jiang and coworkers reported the controllable synthesis of Au nanodendrites.[272] By varying the concentrations of AuNP seed and AA, the length and density of the branches could vary greatly (Fig. 17b). They found that higher density of surface branches exhibited stronger SERS enhancing signals compared to nanostructures with a lower density of surface branches (Fig. 17c and d). The stability of the substrate is also an important indicator. Kelly and coworkers noticed similarly that highly branched structures yield higher sensitivity and lower detection limits.[277] They created a nucleic acid sensor. By comparing the detection limits of three nanostructured microelectrodes (NMEs) (smooth, moderate nanostructuring and fine nanostructuring), it was found that the detection limit of fine NMEs (20–50 nm) was three orders of magnitude lower than that of moderate nanostructuring NMEs (100–300 nm), reaching a sensitivity of 10 aM. This is because the nucleic acid probes on the fine nanostructured electrodes complex faster with the target molecules in solution and they are more accessible.

Nanodendrites also have potential applications in the field of disease diagnosis and health monitoring. If nanodendrites can lead to the identification of previously undetectable biomarkers in clinical samples, it will drive the process of optimizing clinical diagnostic devices.[278] The generally accepted view now is that nanodendritic structures provide numerous hotspots for signal enhancement, which can improve the binding ability and response signal of the probe, thus greatly increasing the sensitivity. For example, Zhang and coworkers achieved simultaneous detection of multiple biomarkers, which on the one hand can shorten the detection time and on the other hand provides for achieving more accurate early diagnosis. They reported that Au nanodendrites can achieve sensitive and selective detection of multiple Alzheimer's biomarkers (including Tau, ApoE4, Amyloid-β and miRNA-101) by improving the probe binding ability and response signal.[279] They can also combine Au nanodendrites and superwettable interfaces for the simultaneous detection of multiple concentrations of miRNAs, minimizing the effects of background signals and the environment.[280] Not only does the hydrophilic interface facilitate signal enhancement, an integrated superhydrophobic–superhydrophilic micropatterning and nanodendritic electrochemical biosensor enables low-dose detection by confining microdroplets in superhydrophilic microwells.[281] Sensitive and selective detection of prostate cancer biomarkers including miRNA-375, miRNA-141, and prostate-specific antigen can be achieved.

Not only that, they also contribute to the detection of food contaminants.[282] A microdroplet-capture tape can be used for rapid SERS screening of food contaminants. The tape-based sensors are loaded with highly branched Au nanodendrites, which are used to enhance the SERS signal. The microdroplets can also be anchored on gloves and can be used to achieve early-warning SERS detection of food contaminants such as Sudan-1, melam, and thiabendazole in real samples by direct dip–pulling sampling. The above works provide a valuable reference for the development of sensitive, stable, and low-cost nanomaterials for biosensors.

4.2.2 Therapy. Active targeting ligands (*e.g.*, antibodies and proteins) can be attached to therapeutic nanodendrites to enhance specific targeting to tumors, so nanodendrites can also be used in the therapeutic field.[283,284] The *in vitro* and *in vivo* studies by Mao and coworkers showed that the Au ND with a higher degree of branching (DB) was more effective in the photothermal tumor destruction under a lower near-infrared (NIR) irradiation than those from higher NIR radiation (Fig. 18a and b).[285] While in the second NIR window, lower DB was better for tumor destruction, suggesting that Au NDs with a lower DB should have better efficiency for photothermal cancer therapy (Fig. 18c). Therefore, the tunable optical properties of Au ND in the NIR range allowed selective determination of an appropriate laser wavelength for optimal cancer treatment. Kim and coworkers synthesized Ag nanodendrites in which ultrafine Pd particles served as seeds that can also be employed as sensitizers for photothermal cancerous cell killing under *in vitro* NIR irradiation.[286] Pan and coworkers proposed a multifoliate PEGylated PtRu bimetallic nanocomplex (PtRu-PEG BNCs) that was used as a multifunctional theranostic nanoagent for computed tomography (CT) imaging and synergistic thermoradiotherapy.[287] The great stability, notable photothermal effect, and excellent biocompatibility indicated that the PtRu-PEG BNCs can be used as multifunctional theranostic nanoagents.

The Pt hollow nanodendrites fabricated by Ge and coworkers showed striking peroxidase-like activity. The Pt hollow nanodendrites catalyzed the decomposition of H_2O_2 into $^{\bullet}OH$ and exhibited excellent bactericidal activity against both Gram-negative and Gram-positive bacteria with the assistance of low concentrations of H_2O_2. Furthermore, Pt hollow nanodendrites accelerated wound healing in the presence of low doses of H_2O_2.[160] Nanodendrite structures also have applications in drug delivery. Msagati and coworkers designed bimetallic gold-core palladium-dendritic shell nanoparticles (Au@PdNDs) stabilized with methoxy polyethylene glycol thiol (mPEG-SH).[288]

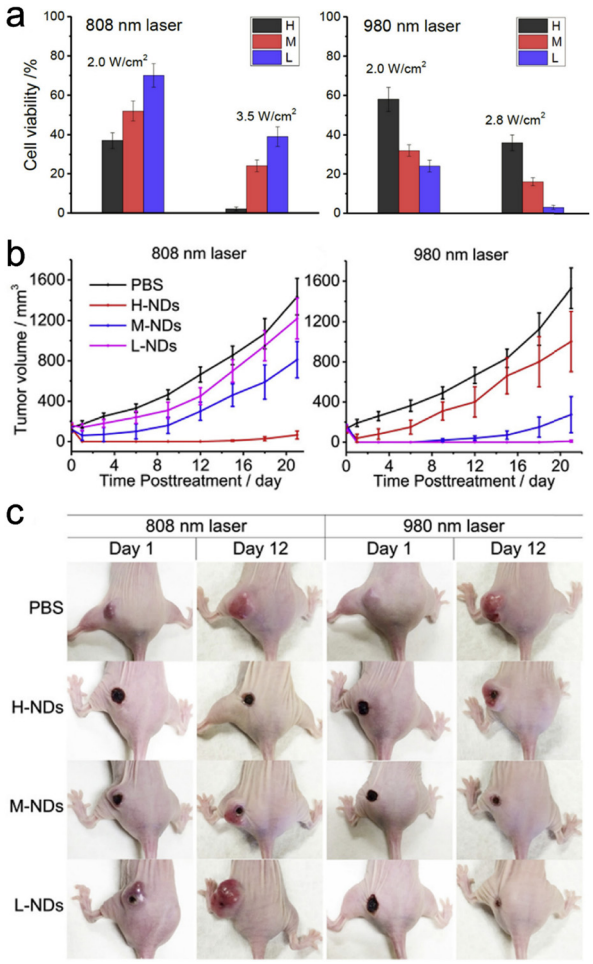

Fig. 18 (a) *In vitro* study of cell viability after irradiation of 808 and 980 nm laser of different power densities. H, M, and L are corresponding to AuNDs of high, medium and low DB, respectively. H-100, H-50 and H-25 in c mean 100, 50 and 25 mg mL^{-1} AuNDs of high DB, respectively, and so as other symbols with the prefix M and L; *in vivo* photothermal treatment of MCF-7 tumors by using AuNDs of different DB; (b) posttreatment tracking of tumor volume in groups treated by 808 nm and 980 nm laser, respectively; (c) photographs of a typical mouse in each group on day 1 and day 12 posttreatment. Adapted with permission from ref. 285. Copyright 2016, Elsevier Ltd.

The experimental results showed that doxorubicin (DOX) has spontaneous heterogeneous binding on the surface of Au@PdNDs, with a maximum adsorption capacity of up to 90% within 24 h. These findings reveal the possibilities of attaching drugs to dendritic carriers for potential drug delivery applications.

Summary and outlook

In the last two decades, with the continuous development of nanotechnology, the study of nanodendrites has been widely reported. From the initial empirical preparation of nanodendrites only to the later mastery of their formation mechanism and the exploration of their applications in numerous fields, it has attracted the wide interest of researchers. This review covers the formation mechanism, synthesis approaches and application of nanodendrites. The formation mechanisms are divided into the fundamental mechanism and several extended mechanisms. The basic mechanisms include the OA mechanism and DLA mechanism, and the extended mechanisms include seed-mediated growth, surfactant-mediated growth, chemical etching growth and other growth. Thanks to the structural characteristics of nanodendrites, they have excellent performance in various fields. This review selects some applications as representatives to highlight the prospects of nanodendrites, mainly summarizing the performance in the HER, ORR, MOR, EOR, and CO_2RR, and biosensing and therapy are also discussed. Promising complex functions are highly dependent on the morphology of the structures. The results show that promising applications with complex functions are highly dependent on the morphology of the structure, and nanodendrites with high exposure density of unsaturated coordination atoms and a large number of highly exposed crystal facets are ideal for the above-mentioned fields.[29]

In order to further develop nanodendrites, the following aspects need to be considered:

(1) The existing formation mechanisms have been refined, and the consensus conclusion is that the branching growth step is a fast step. However, the actual synthesis process is more complex and influenced by many factors, such as the coordination environment of the precursor and the reduction electrode potential of the precursor, which in turn have an impact on the structure of the nanodendrites, so the selection of a suitable preparation parameter must take into account the actual situation.[32,289]

(2) Advances in *in situ* characterization facilitate a deeper and more visualized understanding of the synthesis reaction mechanism, which is very important for achieving the long-term goal of integrated and controlled synthesis of nanodendrites.[290] However, there are still many limitations. Although the growth process can be directly observed with the help of *in situ* TEM, it is based on the strong reducing power of the electron beam as the reducing agent. Its reducing power differs from that of the actual reducing agent used in experiments, therefore, other *in situ* methods should also be explored to help us better understand the formation mechanism.

(3) Theoretical calculations have laid a solid foundation in the field of catalytic mechanism research, providing a reliable source of evidence for exploring reaction process pathways. However, there are fewer related studies in the field of synthesis, and the biggest challenge is that the actual materials are larger and more complex, and the existing techniques are not yet able to directly build models that exactly match the actual materials. Therefore, continues efforts are needed to develop theoretical calculations, which will help us to build a more matching model to gain insight into the formation mechanism of nanodendrites.

(4) The consensus view is that the electronic structure has an important influence on the intrinsic activity of noble metal electrocatalysts. Numerous works have been reported on the modulation of electronic structure, such as loading on carbon

materials, doping with non-metallic/transition metal atoms, changing the phase structure, *etc.* Work related to strain effects has not been reported. The introduction of strain effects in nanodendritic structures requires breaking the nature of noble metal materials and is challenging, but is a direction worth exploring.

(5) Reducing the use of noble metals while maintaining high activity and stability has been a challenge. Nanodendritic materials have achieved the initial goal of exposing as many atoms as possible on the surface, but their usage is still high considering the reduction of commercial costs. The hot topic of a single atom in recent years may be a good entry point to disperse noble metal at atomic levels onto non-noble metal nanodendrites or to select suitable non-noble metal to atomically disperse onto noble metal nanodendrites,[291] which is expected to achieve cost reduction and stability improvement.

(6) Despite the good performance of nanodendrites in electrocatalysis in the last decade, there are still relatively few reports that can be actually applied in fuel cells. The main issue is that the commercialization of the materials needs to consider not only the simplification of the synthesis process but also the ability to maintain high activity and stability in the actually assembled fuel cells.

(7) Noble metal nanodendrites have promising applications in the therapeutic field due to their good stability and biocompatibility. However, their slow metabolism *in vivo* and their poor excretion by the organism limit their clinical translation. Future research directions could turn to the field of noble metal nanodendrites to find more efficient, less toxic, and more rapidly clear inorganic nanomedicines.

Conflicts of interest

There are no conflicts to declare.

Acknowledgements

We are grateful for the financial support from the National Natural Science Foundation of China (22075147 and 21671106), the Priority Academic Program Development of Jiangsu Higher Education Institutions, and the National and Local Joint Engineering Research Center of Biomedical Functional Materials.

References

1 L. Manna, D. J. Milliron, A. Meisel, E. C. Scher and A. P. Alivisatos, *Nat. Mater.*, 2003, **2**, 382–385.
2 C. Y. Yeh, Z. W. Lu, S. Froyen and A. Zunger, *Phys. Rev. B: Condens. Matter Mater. Phys.*, 1992, **46**, 10086–10097.
3 Q. Shen, J. Xue, Y. Li, G. Gao, Q. Li, X. Liu, H. Jia, B. Xu, Y. Wu and S. J. Dillon, *Appl. Catal., B*, 2021, **282**, 119552.
4 T. C. Nanocrystals, L. Manna, E. C. Scher and A. P. Alivisatos, *J. Am. Chem. Soc.*, 2000, **122**, 12700–12706.
5 D. Zitoun, N. Pinna, N. Frolet and C. Belin, *J. Am. Chem. Soc.*, 2006, **127**, 15034–15035.
6 C. R. H. Brune, H. Roder and K. Kern, *Nature*, 1994, **369**, 469–471.
7 H. Fei, J. Dong, D. Chen, T. Hu, X. Duan, I. Shakir, Y. Huang and X. Duan, *Chem. Soc. Rev.*, 2019, **48**, 5207–5241.
8 D. Zhao, Z. Zhuang, X. Cao, C. Zhang, Q. Peng, C. Chen and Y. Li, *Chem. Soc. Rev.*, 2020, **49**, 2215–2264.
9 P. Zhou, X. Hou, Y. Chao, W. Yang, W. Zhang, Z. Mu, J. Lai, F. Lv, K. Yang, Y. Liu, J. Li, J. Ma, J. Luo and S. Guo, *Chem. Sci.*, 2019, **10**, 5898–5905.
10 H. Cheng, R. Gui, H. Yu, C. Wang, S. Liu, H. Liu, T. Zhou, N. Zhang, X. Zheng, W. Chu, Y. Lin, H. Wu, C. Wu and Y. Xie, *Proc. Natl. Acad. Sci. U. S. A.*, 2021, **118**, 2104026118.
11 H. Peng, J. Ren, Y. Wang, Y. Xiong, Q. Wang, Q. Li, X. Zhao, L. Zhan, L. Zheng, Y. Tang and Y. Lei, *Nano Energy*, 2021, **88**, 106307.
12 G. Chen, C. Xu, X. Huang, J. Ye, L. Gu, G. Li, Z. Tang, B. Wu, H. Yang, Z. Zhao, Z. Zhou, G. Fu and N. Zheng, *Nat. Mater.*, 2016, **15**, 564–569.
13 T. Liu, W. Gao, Q. Wang, M. Dou, Z. Zhang and F. Wang, *Angew. Chem., Int. Ed.*, 2020, **59**, 20423–20427.
14 Y. Teng, K. Guo, D. Fan, H. Guo, M. Han, D. Xu and J. Bao, *Chem. – Eur. J.*, 2021, **27**, 11175–11182.
15 C. Zhan, Y. Xu, L. Bu, H. Zhu, Y. Feng, T. Yang, Y. Zhang, Z. Yang, B. Huang, Q. Shao and X. Huang, *Nat. Commun.*, 2021, **12**, 6261.
16 M. Luo, Z. Zhao, Y. Zhang, Y. Sun, Y. Xing, F. Lv, Y. Yang, X. Zhang, S. Hwang, Y. Qin, J. Y. Ma, F. Lin, D. Su, G. Lu and S. Guo, *Nature*, 2019, **574**, 81–85.
17 T. H. Yang, J. Ahn, S. Shi, P. Wang, R. Gao and D. Qin, *Chem. Rev.*, 2021, **121**, 796–833.
18 Z. Che, X. Lu, B. Cai, X. Xu, J. Bao and Y. Liu, *Nano Res.*, 2021, **15**, 1269–1275.
19 J. Wang, H. Yang, F. Li, L. Li, J. Wu, S. Liu, T. Cheng, Y. Xu, Q. Shao and X. Huang, *Sci. Adv.*, 2022, **8**, eabl9271.
20 B. A. Yusuf, W. Yaseen, J. Xie, A. A. Babangida, A. I. Muhammad, M. Xie and Y. Xu, *Nano Energy*, 2022, **104**, 107959.
21 G. A. Somorjai, *Chem. Rev.*, 1996, **96**, 1223–1236.
22 J. Gu, Y. W. Zhang and F. F. Tao, *Chem. Soc. Rev.*, 2012, **41**, 8050–8065.
23 L. Zhang, Y. Wang, J. Li, X. Ren, H. Lv, X. Su, Y. Hu, D. Xu and B. Liu, *ChemCatChem*, 2018, **10**, 4910–4916.
24 H. Huang, A. Cho, S. Kim, H. Jun, A. Lee, J. W. Han and J. Lee, *Adv. Funct. Mater.*, 2020, **30**, 2003889.
25 F. Gao, C. Li, Y. Ren, B. Li, C. Lv, X. Yang, X. Zhang, Z. Lu, X. Yu and L. Li, *Chem. – Eur. J.*, 2022, **28**, e202201860.
26 J. S. Yeon, N. Gupta, P. Bhattacharya and H. S. Park, *Adv. Funct. Mater.*, 2022, **32**, 2112509.
27 S. Wang, J. Xu, W. Li, S. Sun, S. Gao and Y. Hou, *Chem. Rev.*, 2022, **122**, 5411–5475.
28 B. Lim and Y. Xia, *Angew. Chem., Int. Ed.*, 2011, **50**, 76–85.
29 N. K. Chaudhari, J. Joo, H.-b Kwon, B. Kim, H. Y. Kim, S. H. Joo and K. Lee, *Nano Res.*, 2018, **11**, 6111–6140.
30 Y. Yin and A. P. Alivisatos, *Nature*, 2005, **437**, 664–670.
31 M. Hohage, M. Bott, M. Morgenstern, Z. Zhang, T. Michely and G. Comsa, *Phys. Rev. Lett.*, 1996, **76**, 2366–2369.

32 N. Ortiz, J. A. Hammons, S. Cheong and S. E. Skrabalak, *ChemNanoMat*, 2015, **1**, 109–114.
33 M. H. Ullah, W. S. Chung, I. Kim and C. S. Ha, *Small*, 2006, **2**, 870–873.
34 J. Chen, T. Herricks and Y. Xia, *Angew. Chem., Int. Ed.*, 2005, **44**, 2589–2592.
35 B. Jin, Z. Liu, R. Tang and C. Jin, *Chem. Commun.*, 2019, **55**, 8186–8189.
36 L. Shi, A. Wang, T. Zhang, B. Zhang, D. Su, H. Li and Y. Song, *J. Phys. Chem. C*, 2013, **117**, 12526–12536.
37 P. S. Mdluli and N. Revaprasadu, *Mater. Lett.*, 2009, **63**, 447–450.
38 K. Wang, R. Sriphathoorat, S. Luo, M. Tang, H. Du and P. K. Shen, *J. Mater. Chem. A*, 2016, **4**, 13425–13430.
39 D. Zhou, S. Han, Y. Li, N. Ta, Y. Zhou, M. Li, S. Miaoa and W. Shen, *CrystEngComm*, 2021, **23**, 2447–2454.
40 N. Ortiz and S. E. Skrabalak, *Angew. Chem., Int. Ed.*, 2012, **51**, 11757–11761.
41 T. A. Witten and L. M. Sander, *Phys. Rev. Lett.*, 1981, **47**, 1400–1403.
42 D. Xu, H. Lv, H. Jin, Y. Liu, Y. Ma, M. Han, J. Bao and B. Liu, *J. Phys. Chem. Lett.*, 2019, **10**, 663–671.
43 Y. Hayakawa, S. Sato and M. Matsushita, *Phys. Rev. A*, 1987, **36**, 1963–1966.
44 M. Matsushita, M. Sano, Y. Hayakawa, H. Honjo and Y. Sawada, *Phys. Rev. Lett.*, 1984, **53**, 286–289.
45 R. M. Brady and R. C. Ball, *Nature*, 1984, **309**, 225–230.
46 Epameinondas Leontidis, Konstantina Kleitou, Tasoula Kyprianidou-Leodidou, Vlasoula Bekiari and P. Lianos, *Langmuir*, 2002, **18**, 3659–3668.
47 S. Wang and H. Xin, *J. Phys. Chem. B*, 2000, **104**, 5681–5685.
48 M. Kolb, R. Botet and R. Jullien, *Phys. Rev. Lett.*, 1983, **51**, 1123–1126.
49 P. Meakin, *Phys. Rev. Lett.*, 1983, **51**, 1119–1122.
50 L. M. Sander, *Contemp. Phys.*, 2000, **41**, 203–218.
51 S. Pang, T. Kondo and T. Kawai, *Chem. Mater.*, 2005, **17**, 3636–3641.
52 R. L. Penn and J. F. Banfield, *Science*, 1998, **281**, 969–971.
53 X. Teng, S. Maksimuk, S. Frommer and H. Yang, *Chem. Mater.*, 2007, **19**, 36–41.
54 H. Kobayashi, B. Lim, J. Wang, P. H. C. Camargo, T. Yu, M. J. Kim and Y. Xia, *Chem. Phys. Lett.*, 2010, **494**, 249–254.
55 B. Lim, M. Jiang, P. H. C. Camargo, E. C. Cho, J. Tao, X. Lu, Y. Zhu and Y. Xia, *Science*, 2009, **324**, 1302–1305.
56 L. Wang and Y. Yamauchi, *Chem. Mater.*, 2009, **21**, 3562–3569.
57 Y. Song, Y. Yang, C. J. Medforth, E. Pereira, A. K. Singh, H. Xu, Y. Jiang, C. J. Brinker, F. Swol and J. A. Shelnutt, *J. Am. Chem. Soc.*, 2004, **126**, 635–645.
58 J. E. Evans, K. L. Jungjohann, N. D. Browning and I. Arslan, *Nano Lett.*, 2011, **11**, 2809–2813.
59 H. Zheng, R. K. Smith, Y. W. Jun, C. Kisielowski, U. Dahmen and A. P. Alivisatos, *Science*, 2009, **324**, 1309–1312.
60 C. H. B. Ng and W. Y. Fan, *Cryst. Growth Des.*, 2014, **14**, 6067–6072.
61 H. You, S. Yang, B. Ding and H. Yang, *Chem. Soc. Rev.*, 2013, **42**, 2880–2904.
62 H. G. Liao, L. Cui, S. Whitelam and H. Zheng, *Science*, 2012, **336**, 1011–1014.
63 S. Lu, K. Eid, D. Ge, J. Guo, L. Wang, H. Wang and H. Gu, *Nanoscale*, 2017, **9**, 1033–1039.
64 H. Wu, S. Mei, X. Cao, J. Zheng, M. Lin, J. Tang, F. Ren, Y. Du, Y. Pan and H. Gu, *Nanotechnology*, 2014, **25**, 195702.
65 X. Wen, Y. Xie, M. W. C. Mak, K. Y. Cheung, X. Li, R. Renneberg and S. Yang, *Langmuir*, 2006, **22**, 4836–4842.
66 M. V. Brink, M. A. Peck, K. L. More and J. D. Hoefelmeyer, *J. Phys. Chem. C*, 2008, **112**, 12122–12126.
67 Z. Aabdin, J. Lu, X. Zhu, U. Anand, N. D. Loh, H. Su and U. Mirsaidov, *Nano Lett.*, 2014, **14**, 6639–6643.
68 S. Zhang, H. Rong, T. Yang, B. Bai and J. Zhang, *Chem. – Eur. J.*, 2019, **26**, 4025–4031.
69 L. Gloag, T. M. Benedetti, S. Cheong, Y. Li, X. H. Chan, L. M. Lacroix, S. L. Y. Chang, R. Arenal, I. Florea, H. Barron, A. S. Barnard, A. M. Henning, C. Zhao, W. Schuhmann, J. J. Gooding and R. D. Tilley, *Angew. Chem., Int. Ed.*, 2018, **57**, 10241–10245.
70 J. Zhang, J. Ye, Q. Fan, Y. Jiang, Y. Zhu, H. Li, Z. Cao, Q. Kuang, J. Cheng, J. Zheng and Z. Xie, *J. Am. Chem. Soc.*, 2018, **140**, 11232–11240.
71 Z. Niu, D. Wang, R. Yu, Q. Peng and Y. Li, *Chem. Sci.*, 2012, **3**, 1925.
72 B. Lim, M. Jiang, T. Yu, P. H. C. Camargo and Y. Xia, *Nano Res.*, 2010, **3**, 69–80.
73 Y. Feng, H. Liu and J. Yang, *J. Mater. Chem. A*, 2014, **2**, 6130–6137.
74 S. Maksimuk, X. Teng and H. Yang, *J. Phys. Chem. C*, 2007, **111**, 14312–14319.
75 M. Song, G. Zhou, N. Lu, J. Lee, E. Nakouzi, H. Wang and D. Li, *Science*, 2020, **367**, 40–45.
76 F. Gao, Y. Zhang, P. Song, J. Wang, C. Wang, J. Guo and Y. Du, *J. Power Sources*, 2019, **418**, 186–192.
77 H. Lv, Y. Teng, Y. Wang, D. Xu and B. Liu, *Chem. Commun.*, 2020, **56**, 15667–15670.
78 H. Lv, L. Sun, D. Xu, S. L. Suib and B. Liu, *Green Chem.*, 2019, **21**, 2367–2374.
79 H. Zou, B. Jin, R. Wang, Y. Wu, H. Yang and S. Qiu, *J. Mate. Chem. A*, 2018, **6**, 24166–24174.
80 M. Gong, X. Jiang, T. Xue, T. Shen, L. Xu, D. Sun and Y. Tang, *Catal. Sci. Technol.*, 2015, **5**, 5105–5109.
81 Y. Zheng, Y. Ma, G. Zhang, W. Zhao, F. Liu and M. Liu, *CrystEngComm*, 2021, **23**, 6879–6891.
82 W. Si, J. Li, H. Li, S. Li, J. Yin, H. Xu, X. Guo, T. Zhang and Y. Song, *Nano Res.*, 2013, **6**, 720–725.
83 D. Xu, X. Liu, H. Lv, Y. Liu, S. Zhao, M. Han, J. Bao, J. He and B. Liu, *Chem. Sci.*, 2018, **9**, 4451–4455.
84 Y. Zhou, D. Wang and Y. Li, *Chem. Commun.*, 2014, **50**, 6141–6144.
85 L. Zhang, X. F. Zhang, X. L. Chen, A. J. Wang, D. M. Han, Z. G. Wang and J. J. Feng, *J. Colloid Interface Sci.*, 2019, **536**, 556–562.

86 G. Fu, K. Wu, J. Lin, Y. Tang, Y. Chen, Y. Zhou and T. Lu, *J. Phys. Chem. C*, 2013, **117**, 9826–9834.
87 J. Gao, Cr. M. Bender and C. J. Murphy, *Langmuir*, 2003, **19**, 9065–9070.
88 G. Su, H. Jiang, H. Zhu, J. J. Lv, G. Yang, B. Yan and J. J. Zhu, *Nanoscale*, 2017, **9**, 12494–12502.
89 K. Guo, D. Fan, Y. Teng, D. Xu, Y. Li and J. Bao, *Chem. – Eur. J.*, 2022, **28**, e202200053.
90 X. Han, D. Wang, D. Liu, J. Huang and T. You, *J. Colloid Interface Sci.*, 2012, **367**, 342–347.
91 C. J. Johnson, E. Dujardin, S. A. Davis, C. J. Murphy and S. Mann, *J. Mater. Chem.*, 2002, **12**, 1765–1770.
92 W. Huang, X. Kang, C. Xu, J. Zhou, J. Deng, Y. Li and S. Cheng, *Adv. Mater.*, 2018, **30**, 1706962.
93 D. Huang, X. Bai and L. Zheng, *J. Phys. Chem. C*, 2011, **115**, 14641–14647.
94 T. Huang, F. Meng and L. Qi, *Langmuir*, 2010, **26**, 7582–7589.
95 B. K. Jena and C. R. Raj, *Langmuir*, 2007, **23**, 4064–4070.
96 X. Wen, S. Lerch, Z. Wang, B. Aboudiab, A. R. Tehrani-Bagha, E. Olsson and K. Moth-Poulsen, *Langmuir*, 2020, **36**, 1745–1753.
97 Z. H. Lin, M. H. Lin and H. T. Chang, *Chem. – Eur. J.*, 2009, **15**, 4656–4662.
98 V. T. Kelleppan, J. P. King, C. S. G. Butler, A. P. Williams, K. L. Tuck and R. F. Tabor, *Adv. Colloid Interface Sci.*, 2021, **297**, 102528.
99 A. Wu, Y. Gao and L. Zheng, *Green Chem.*, 2019, **21**, 4290–4312.
100 H. Lu, C. Zheng, M. Xue and Z. Huang, *Phys. Chem. Chem. Phys.*, 2016, **18**, 32192–32197.
101 L. Wang, M. Imura and Y. Yamauchi, *ACS Appl. Mater. Interfaces*, 2012, **4**, 2865–2869.
102 L. Wang and Y. Yamauchi, *Chem. – Eur. J.*, 2011, **17**, 8810–8815.
103 L. Wang and Y. Yamauchi, *J. Am. Chem. Soc.*, 2009, **131**, 9152–9153.
104 L. Wang, Y. Nemoto and Y. Yamauchi, *J. Am. Chem. Soc.*, 2011, **133**, 9674–9677.
105 H. Liu, J. Qin, S. Zhao, Z. Gao, Q. Fu and Y. Song, *Electrochem. Commun.*, 2019, **98**, 53–57.
106 X. Wang, H. Itoh, K. Naka and Y. Chujo, *Langmuir*, 2003, **19**, 6242–6246.
107 Y. Xiong, W. Ye, W. Chen, Y. Wu, Q. Xu, Y. Yan, H. Zhang, J. Wu and D. Yang, *RSC Adv.*, 2017, **7**, 5800–5806.
108 Q. Wang, Y. Li, B. Liu, G. Xu, G. Zhang, Q. Zhao and J. Zhang, *J. Power Sources*, 2015, **297**, 59–67.
109 L. Sun, A. Liu, X. Tao and Y. Zhao, *J. Mater. Sci.*, 2010, **46**, 839–845.
110 M. A. Mahmoud, C. E. Tabor, M. A. El-Sayed, Y. Ding and Z. L. Wang, *J. Am. Chem. Soc.*, 2008, **130**, 4590–4591.
111 Y. Cao, Y. Yang, Y. Shan and Z. Huang, *ACS Appl. Mater. Interfaces*, 2016, **8**, 5998–6003.
112 Y. Kang, F. Li, S. Li, P. Ji, J. Zeng, J. Jiang and Y. Chen, *Nano Res.*, 2016, **9**, 3893–3902.
113 Z. Q. Zhang, J. Huang, L. Zhang, M. Sun, Y. C. Wang, Y. Lin and J. Zeng, *Nanotechnology*, 2014, **25**, 435602.
114 X. Teng, X. Liang, S. Maksimuk and H. Yang, *Small*, 2006, **2**, 249–253.
115 J. Watt, S. Cheong, M. F. Toney, B. Ingham, J. Cookson, P. T. Bishop and R. D. Tilley, *ACS Nano*, 2010, **4**, 396–402.
116 A. Shan, S. Huang, H. Zhao, W. Jiang, X. Teng, Y. Huang, C. Chen, R. Wang and W. M. Lau, *Nano Res.*, 2020, **13**, 3088–3097.
117 H. Wang, B. Zeng, Y. Zhao, M. Li, H. Liu and T. Huang, *J. Nanosci. Nanotechnol.*, 2018, **18**, 730–734.
118 X. J. Liu, C. H. Cui, M. Gong, H. H. Li, Y. Xue, F. J. Fan and S. H. Yu, *Chem. Commun.*, 2013, **49**, 8704–8706.
119 W. Wang, D. Wang, X. Liu, Q. Peng and Y. Li, *Chem. Commun.*, 2013, **49**, 2903–2905.
120 X. Liu, W. Wang, H. Li, L. Li, G. Zhou, R. Yu, D. Wang and Y. Li, *Sci. Rep.*, 2013, **3**, 1404.
121 J. N. Zheng, L. He, F. Chen, A. Wang, M. Xue and J. Feng, *J. Mater. Chem. A*, 2014, **2**, 12899–12906.
122 L. Wang, H. Wang, Y. Nemoto and Y. Yamauchi, *Chem. Mater.*, 2010, **22**, 2835–2841.
123 A. Abdelhafiz, B. Zhao, Z. Xiao, J. Zeng, X. Deng, L. Lang, Y. Ding, H. Song and M. Liu, *ACS Appl. Mater. Interfaces*, 2020, **12**, 49510–49518.
124 L. Wang, C. Hu, Y. Nemoto, Y. Tateyama and Y. Yamauchi, *Cryst. Growth Des.*, 2010, **10**, 3454–3460.
125 A. Mohanty, N. Garg and R. Jin, *Angew. Chem., Int. Ed.*, 2010, **49**, 4962–4966.
126 H. Wu, P. Wang, H. He and Y. Jin, *Nano Res.*, 2012, **5**, 135–144.
127 Y. Xiong, B. Wiley, J. Chen, Z. Y. Li, Y. Yin and Y. Xia, *Angew. Chem., Int. Ed.*, 2005, **44**, 7913–7917.
128 L. Au, Y. Chen, F. Zhou, P. H. Camargo, B. Lim, Z. Y. Li, D. S. Ginger and Y. Xia, *Nano Res.*, 2008, **1**, 441–449.
129 S. Xie, N. Lu, Z. Xie, J. Wang, M. J. Kim and Y. Xia, *Angew. Chem., Int. Ed.*, 2012, **51**, 10266–10270.
130 E. Taylor, S. Chen, J. Tao, L. Wu, Y. Zhu and J. Chen, *ChemSusChem*, 2013, **6**, 1863–1867.
131 Y. Yan, X. Li, M. Tang, H. Zhong, J. Huang, T. Bian, Y. Jiang, Y. Han, H. Zhang and D. Yang, *Adv. Sci.*, 2018, **5**, 1800430.
132 H. Huang, A. Ruditskiy, S. I. Choi, L. Zhang, J. Liu, Z. Ye and Y. Xia, *ACS Appl. Mater. Interfaces*, 2017, **9**, 31203–31212.
133 F. Nosheen, Z. Zhang, G. Xiang, B. Xu, Y. Yang, F. Saleem, X. Xu, J. Zhang and X. Wang, *Nano Res.*, 2015, **8**, 832–838.
134 M. Gong, G. Fu, Y. Chen, Y. Tang and T. Lu, *ACS Appl. Mater. Interfaces*, 2014, **6**, 7301–7308.
135 L. Wang and Y. Yamauchi, *J. Am. Chem. Soc.*, 2013, **135**, 16762–16765.
136 A. J. Wang, F. F. Li, Z. Bai and J. J. Feng, *Electrochim. Acta*, 2012, **85**, 685–692.
137 J. J. Feng, A. Q. Li, Z. Lei and A. J. Wang, *ACS Appl. Mater. Interfaces*, 2012, **4**, 2570–2576.
138 X. Qin, Z. Miao, Y. Fang, D. Zhang, J. Ma, L. Zhang, Q. Chen and X. Shao, *Langmuir*, 2012, **28**, 5218–5226.

139 X. Qin, H. Wang, X. Wang, Z. Miao, Y. Fang, Q. Chen and X. Shao, *Electrochim. Acta*, 2011, **56**, 3170–3174.
140 J. Xiao, Y. Xie, R. Tang, M. Chen and X. Tian, *Adv. Mater.*, 2001, **13**, 1887–1891.
141 P. N. Vakil, D. A. Hardy and G. F. Strouse, *ACS Nano*, 2018, **12**, 6784–6793.
142 N. Li, S. Tang, Y. Pan and X. Meng, *Mater. Res. Bull.*, 2014, **49**, 119–125.
143 P. Zhou, Z. Dai, M. Fang, X. Huang, J. Bao and J. Gong, *J. Phys. Chem. C*, 2007, **111**, 12609–12616.
144 L. Wang, J. Wen, H. Sheng and D. J. Miller, *Nanoscale*, 2016, **8**, 17250–17255.
145 M. Wang, C. Park and T. J. Woehl, *Chem. Mater.*, 2018, **30**, 7727–7736.
146 M. R. Hauwiller, X. Zhang, W. I. Liang, C. H. Chiu, Q. Zhang, W. Zheng, C. Ophus, E. M. Chan, C. Czarnik, M. Pan, F. M. Ross, W. W. Wu, Y. H. Chu, M. Asta, P. W. Voorhees, A. P. Alivisatos and H. Zheng, *Nano Lett.*, 2018, **18**, 6427–6433.
147 Y. Chen, Z. Fan, Z. Zhang, W. Niu, C. Li, N. Yang, B. Chen and H. Zhang, *Chem. Rev.*, 2018, **118**, 6409–6455.
148 X. Huang, S. Tang, X. Mu, Y. Dai, G. Chen, Z. Zhou, F. Ruan, Z. Yang and N. Zheng, *Nat. Nanotechnol.*, 2011, **6**, 28–32.
149 W. Lu, X. Xia, X. Wei, M. Li, M. Zeng, J. Guo and S. Cheng, *ACS Appl. Mater. Interfaces*, 2020, **12**, 21569–21578.
150 K. Guo, Y. Liu, M. Han, D. Xu and J. Bao, *Chem. Commun.*, 2019, **55**, 11131–11134.
151 Q. Yao, B. Huang, N. Zhang, M. Sun, Q. Shao and X. Huang, *Angew. Chem., Int. Ed.*, 2019, **58**, 13983–13988.
152 X. F. Zhang, X. Y. Zhu, J. J. Feng and A. J. Wang, *Appl. Surf. Sci.*, 2018, **428**, 798–808.
153 Z. Cai, C. Liu, G. Wu, X. Chen and X. Chen, *Electrochim. Acta*, 2014, **127**, 377–383.
154 H. S. Oh, H. N. Nong, T. Reier, M. Gliech and P. Strasser, *Chem. Sci.*, 2015, **6**, 3321–3328.
155 Z. Zhao, M. M. Flores Espinosa, J. Zhou, W. Xue, X. Duan, J. Miao and Y. Huang, *Nano Res.*, 2019, **12**, 1467–1472.
156 H. Y. Sun, Y. Ding, Y. Q. Yue, Q. Xue, F. M. Li, J. X. Jiang, P. Chen and Y. Chen, *ACS Appl. Mater. Interfaces*, 2021, **13**, 13149–13157.
157 F. Lv, J. Feng, K. Wang, Z. Dou, W. Zhang, J. Zhou, C. Yang, M. Luo, Y. Yang, Y. Li, P. Gao and S. Guo, *ACS Cent. Sci.*, 2018, **4**, 1244–1252.
158 Y. Ge, X. Wang, B. Chen, Z. Huang, Z. Shi, B. Huang, J. Liu, G. Wang, Y. Chen, L. Li, S. Lu, Q. Luo, Q. Yun and H. Zhang, *Adv. Mater.*, 2022, **34**, 2107399.
159 K. Eid, Y. H. Ahmad, H. Yu, Y. Li, X. Li, S. Y. AlQaradawi, H. Wang and L. Wang, *Nanoscale*, 2017, **9**, 18881–18889.
160 R. Wu, Y. Chong, G. Fang, X. Jiang, Y. Pan, C. Chen, J. Yin and C. Ge, *Adv. Funct. Mater.*, 2018, **28**, 1801484.
161 X. Zhu, L. Huang, M. Wei, P. Tsiakaras and P. K. Shen, *Appl. Catal., B*, 2021, **281**, 119460.
162 X.-R. Li, X. L. Li, M. C. Xu, J. J. Xu and H. Y. Chen, *J. Mater. Chem. A*, 2014, **2**, 1697–1703.
163 L. Huang, Y. Han and S. Dong, *Chem. Commun.*, 2016, **52**, 8659–8662.
164 J. J. Lv, N. Wisitruangsakul, J. J. Feng, J. Luo, K. M. Fang and A. J. Wang, *Electrochim. Acta*, 2015, **160**, 100–107.
165 S. S. Li, Y. Y. Hu, J. J. Feng, Z. Y. Lv, J. R. Chen and A. J. Wang, *Int. J. Hydrogen Energy*, 2014, **39**, 3730–3738.
166 C. Yang, Q. Jiang, H. Liu, L. Yang, H. He, H. Huang and W. Li, *J. Mater. Chem. A*, 2021, **9**, 15432–15440.
167 M. T. Tajabadi, W. J. Basirun, F. Lorestani, R. Zakaria, S. Baradaran, Y. M. Amin, M. R. Mahmoudian, M. Rezayi and M. Sookhakian, *Electrochim. Acta*, 2015, **151**, 126–133.
168 M. Li, Q. Kong, Z. Bian, C. Ma, S. Ge, Y. Zhang, J. Yu and M. Yan, *Biosens. Bioelectron.*, 2015, **65**, 176–182.
169 X. Chen, B. Su, Z. Cai, X. Chen and M. Oyama, *Sens. Actuators, B*, 2014, **201**, 286–292.
170 F. Liu, G. Xiang, D. Jiang, L. Zhang, X. Chen, L. Liu, F. Luo, Y. Li, C. Liu and X. Pu, *Biosens. Bioelectron.*, 2015, **74**, 214–221.
171 S. J. Ye, D. Y. Kim, D. W. Kim, O. O. Park and Y. Kang, *J. Mater. Chem. A*, 2016, **4**, 578–586.
172 X. Huang, Y. Li, Y. Chen, E. Zhou, Y. Xu, H. Zhou, X. Duan and Y. Huang, *Angew. Chem., Int. Ed.*, 2013, **52**, 2520–2524.
173 L. Zhou, Z. Liu, H. Zhang, S. Cheng, L. J. Fan and W. Ma, *Nanoscale*, 2014, **6**, 12971–12980.
174 W. Zhang, F. Tan, W. Wang, X. Qiu, X. Qiao and J. Chen, *J. Hazard. Mater.*, 2012, **217–218**, 36–42.
175 L. Yang, Y. Li, Y. Zhang, D. Fan, X. Pang, Q. Wei and B. Du, *ACS Appl. Mater. Interfaces*, 2017, **9**, 35260–35267.
176 R. Yang, Y. Wang, D. Wu, Y. Deng, Y. Luo, X. Cui, X. Wang, Z. Shu and C. Yang, *ACS Nano*, 2017, **11**, 7710–7718.
177 J. F. Hu, J. Z. Sun, C. Bian, J. H. Tong and S. H. Xia, *Key Eng. Mater.*, 2013, **562–565**, 652–657.
178 Z. Khorablou, F. Shahdost-fard and H. Razmi, *Surf. Interfaces*, 2022, **31**, 102061.
179 J. J. Lv, A. J. Wang, X. Ma, R. Y. Xiang, J. R. Chen and J. J. Feng, *J. Mater. Chem. A*, 2015, **3**, 290–296.
180 Z. J. Wang, J. J. Lv, J. J. Feng, N. Li, X. Xu, A. J. Wang and R. Qiu, *RSC Adv.*, 2015, **5**, 28467–28473.
181 L. Jiao, L. Zhang, W. Du, H. Li, D. Yang and C. Zhu, *Nanoscale*, 2019, **11**, 8798–8802.
182 Y. X. Xiao, J. Ying, G. Tian, X. Yang, Y. X. Zhang, J. B. Chen, Y. Wang, M. D. Symes, K. I. Ozoemena, J. Wu and X. Y. Yang, *Nano Lett.*, 2021, **21**, 7870–7878.
183 Y. Lu, S. Du and R. Steinberger-Wilckens, *Appl. Catal., B*, 2016, **187**, 108–114.
184 G. R. Xu, J. Bai, J. X. Jiang, J. M. Lee and Y. Chen, *Chem. Sci.*, 2017, **8**, 8411–8418.
185 X. F. Zhang, Y. Chen, L. Zhang, A. J. Wang, L. J. Wu, Z. G. Wang and J. J. Feng, *J. Colloid Interface Sci.*, 2018, **516**, 325–331.
186 Z. Han, R. L. Zhang, J. J. Duan, A. J. Wang, Q. L. Zhang, H. Huang and J. J. Feng, *Int. J. Hydrogen Energy*, 2020, **45**, 6110–6119.
187 X. Weng, Y. Liu, K. K. Wang, J. J. Feng, J. Yuan, A. J. Wang and Q. Q. Xu, *Int. J. Hydrogen Energy*, 2016, **41**, 18193–18202.

188 H. Y. Chen, A. J. Wang, L. Zhang, J. Yuan, Q. L. Zhang and J. J. Feng, *Int. J. Hydrogen Energy*, 2018, **43**, 22187–22194.
189 L. Li, S. Wang, L. Xiong, B. Wang, G. Yang and S. Yang, *J. Mater. Chem. A*, 2019, **7**, 12800–12807.
190 Y. H. Lai, S. R. Li, M. G. Swathi, H. T. Chang, Y. B. Huang, Y. K. Li, Y. M. Chen, S. B. Patil, S. Y. Chang, P. K. Chen, C. C. Chang, Y. C. Chen, C. W. Pao, J. L. Chen, C. Y. Wei, I. K. Lin, H. L. Chou, C. J. Su, U. S. Jeng, T.-R. Kuo, C. Y. Wen and D. Y. Wang, *J. Mater. Chem. A*, 2021, **9**, 22901–22912.
191 Z. Z. Yang, X. X. Lin, X. F. Zhang, A. J. Wang, X. Y. Zhu and J. J. Feng, *J. Alloys Compd.*, 2018, **735**, 2123–2132.
192 Z. He, H. Wang, T. Yu, L. Zuo, S. Yan, T. Bian and S. Su, *ChemistrySelect*, 2022, **7**, e202103472.
193 Q. Liu, C. Fan, X. Zhou, J. Liu, S. Jiang, S. Wang, X. Wang and Y. Tang, *New J. Chem.*, 2020, **44**, 21021–21025.
194 Y. X. Xie, S. Y. Cen, Y. T. Ma, H. Y. Chen, A. J. Wang and J. J. Feng, *J. Colloid Interface Sci.*, 2020, **579**, 250–257.
195 K. Gao, Y. Wang, Z. Wang, Z. Zhu, J. Wang, Z. Luo, C. Zhang, X. Huang, H. Zhang and W. Huang, *Chem. Commun.*, 2018, **54**, 4613–4616.
196 Y. C. Jiang, H. Y. Sun, Y. N. Li, J. W. He, Q. Xue, X. Tian, F. M. Li, S. B. Yin, D. S. Li and Y. Chen, *ACS Appl. Mater. Interfaces*, 2021, **13**, 35767–35776.
197 V. R. Stamenkovic, B. Fowler, B. S. Mun, G. Wang, P. N. Ross, C. A. Lucas and N. M. Marković, *Science*, 2007, **315**, 493–497.
198 Y. Liao, J. Li, S. Zhang and S. Chen, *Chin. J. Catal.*, 2021, **42**, 1108–1116.
199 D. Y. Wang, H. L. Chou, C. C. Cheng, Y. H. Wu, C. M. Tsai, H. Y. Lin, Y. L. Wang, B. J. Hwang and C. C. Chen, *Nano Energy*, 2015, **11**, 631–639.
200 S. Fu, C. Zhu, J. Song, P. Zhang, M. H. Engelhard, H. Xia, D. Du and Y. Lin, *Nanoscale*, 2017, **9**, 1279–1284.
201 G. Zhang, Z.-G. Shao, W. Lu, F. Xie, X. Qin and B. Yi, *Electrochim. Acta*, 2013, **103**, 66–76.
202 Z. An, H. Li, X. Zhang, X. Xu, Z. Xia, S. Yu, W. Chu, S. Wang and G. Sun, *ACS Catal.*, 2022, **12**, 3302–3308.
203 Y. Liao, J. Li, S. Zhang and S. Chen, *Chin. J. Catal.*, 2021, **42**, 1108–1116.
204 V. S. Bagotzky, Y. B. Vassiliev and O. A. Khazova, *J. Electroanal. Chem.*, 1977, **81**, 229–238.
205 J. P. Zhong, C. Hou, L. Li, M. Waqas, Y. J. Fan, X. C. Shen, W. Chen, L. Y. Wan, H. G. Liao and S. G. Sun, *J. Catal.*, 2020, **381**, 275–284.
206 C. Shang, Y. Guo and E. Wang, *J. Mater. Chem. A*, 2019, **7**, 2547–2552.
207 D. Cao, G. Q. Lu, A. Wieckowski and M. Neurock, *J. Phys. Chem. B*, 2005, **109**, 11622–11633.
208 R. Sriphathoorat, K. Wang and P. K. Shen, *ACS Appl. Energy Mater.*, 2019, **2**, 961–965.
209 A. Cheng, Y. Wang, L. Ma, L. Lin and H. Zhou, *Nanotechnology*, 2020, **31**, 435403.
210 K. Eid, H. Wang, V. Malgras, S. M. Alshehri, T. Ahamad, Y. Yamauchi and L. Wang, *J. Electroanal. Chem.*, 2016, **779**, 250–255.
211 P. Song, L. Liu, J. J. Feng, J. Yuan, A. J. Wang and Q. Q. Xu, *Int. J. Hydrogen Energy*, 2016, **41**, 14058–14067.
212 H. Kwon, M. K. Kabiraz, J. Park, A. Oh, H. Baik, S. I. Choi and K. Lee, *Nano Lett.*, 2018, **18**, 2930–2936.
213 L. Guo, L. B. Huang, W. J. Jiang, Z. D. Wei, L. J. Wan and J. S. Hu, *J. Mater. Chem. A*, 2017, **5**, 9014–9021.
214 S. Fu, C. Zhu, Q. Shi, H. Xia, D. Du and Y. Lin, *Nanoscale*, 2016, **8**, 5076–5081.
215 D. Chen, P. Sun, H. Liu and J. Yang, *J. Mater. Chem. A*, 2017, **5**, 4421–4429.
216 L. Xiong, Y. X. Huang, X. W. Liu, G. P. Sheng, W. W. Li and H. Q. Yu, *Electrochim. Acta*, 2013, **89**, 24–28.
217 T. Song, H. Xue, N. Guo, J. Sun, L. Qin, L. Guo, K. Huang, F. He and Q. Wang, *Chem. Commun.*, 2020, **56**, 7136–7139.
218 R. Chen, Z. Cao, Z. Lyu, M. Xie, Y. Shi and Y. Xia, *ChemNanoMat*, 2019, **5**, 599–605.
219 R. Wu, Y. Li, W. Gong and P. K. Shen, *ACS Sustainable Chem. Eng.*, 2019, **7**, 8419–8428.
220 W. Lei, M. Li, L. He, X. Meng, Z. Mu, Y. Yu, F. M. Ross and W. Yang, *Nano Res.*, 2020, **13**, 638–645.
221 Y. Tan, J. Fan, G. Chen, N. Zheng and Q. Xie, *Chem. Commun.*, 2011, **47**, 11624–11626.
222 J. N. Tiwari, K. C. Kemp, K. Nath, R. N. Tiwari, H.-G. Nam and K. S. Kim, *ACS Nano*, 2013, **7**, 9223–9231.
223 L. B. Venarusso, C. V. Boone, J. Bettini and G. Maia, *J. Mater. Chem. A*, 2018, **6**, 1714–1726.
224 J. Wang, F. Chen, Y. Jin, Y. Lei and R. L. Johnston, *Adv. Funct. Mater.*, 2017, **27**, 1700260.
225 K. Eid, H. Wang, V. Malgras, Z. A. Alothman, Y. Yamauchi and L. Wang, *J. Phys. Chem. C*, 2015, **119**, 19947–19953.
226 Q. Liu, Q. Kang, Z. Wang, Q. Lu and F. Gao, *Dalton Trans.*, 2021, **50**, 6297–6305.
227 S. Wang, D. Tian, X. Wang, J. Qin, Y. Tang, J. Zhu, Y. Cong, H. Liu, Y. Lv, C. Qiu, Z. Gao and Y. Song, *Electrochem. Commun.*, 2019, **102**, 67–71.
228 Y. Qi, J. Wu, H. Zhang, Y. Jiang, C. Jin, M. Fu, H. Yang and D. Yang, *Nanoscale*, 2014, **6**, 7012–7018.
229 R. Xie, S. Lu, Y. Deng, S. Mei, X. Cao, L. Zhou, C. Lan and H. Gu, *Inorg. Chem.*, 2019, **58**, 5375–5379.
230 L. Lu, S. Chen, S. Thota, X. Wang, Y. Wang, S. Zou, J. Fan and J. Zhao, *J. Phys. Chem. C*, 2017, **121**, 19796–19806.
231 M. Li, H. Zheng, G. Han, Y. Xiao and Y. Li, *Catal. Commun.*, 2017, **92**, 95–99.
232 J. Liu, L. Cao, W. Huang and Z. Li, *J. Electroanal. Chem.*, 2012, **686**, 38–45.
233 Z. Li, Z. Guan, Y. Chang, D. Hu, B. Jin and L. Bai, *CrystEngComm*, 2020, **22**, 1442–1447.
234 R. Chang, L. Zheng, C. Wang, D. Yang, G. Zhang and S. Sun, *Appl. Catal., B*, 2017, **211**, 205–211.
235 Z. Cai, Y. Kuang, X. Qi, P. Wang, Y. Zhang, Z. Zhang and X. Sun, *J. Mater. Chem. A*, 2015, **3**, 1182–1187.
236 Y. Fan, P. F. Liu, Z. Y. Huang, T. W. Jiang, K. L. Yao and R. Han, *J. Power Sources*, 2015, **280**, 30–38.
237 S. Guo, S. Dong and E. Wang, *ACS Nano*, 2010, **4**, 547–555.
238 W. Yuan, X. Fan, Z. M. Cui, T. Chen, Z. Dong and C. M. Li, *J. Mater. Chem. A*, 2016, **4**, 7352–7364.
239 Y. Li, W. Ding, M. Li, H. Xia, D. Wang and X. Tao, *J. Mater. Chem. A*, 2015, **3**, 368–376.

240 T. Zhang, Y. Sun, X. Li, X. Li, D. Liu, G. Liu, C. Li, H. J. Fan and Y. Li, *Small Methods*, 2019, **4**, 1900709.
241 B. Sun, L. Huang, S. Su, S. Luo, C. Meng, H. M. A. Basit, J. Xiao, T. Bian and S. Su, *Mater. Chem. Phys.*, 2020, **252**, 123234.
242 S. C. Sahu, A. K. Samantara, A. Dash, R. R. Juluri, R. K. Sahu, B. K. Mishra and B. K. Jena, *Nano Res.*, 2013, **6**, 635–643.
243 J. J. Feng, L. X. Chen, X. Ma, J. Yuan, J. R. Chen, A. J. Wang and Q. Q. Xu, *Int. J. Hydrogen Energy*, 2017, **42**, 1120–1129.
244 F. Wu, L. Zhang, J. Lai, W. Niu, R. Luque and G. Xu, *J. Mater. Chem. A*, 2019, **7**, 8568–8572.
245 J. J. Lv, J. N. Zheng, S. S. Li, L. L. Chen, A. J. Wang and J. J. Feng, *J. Mater. Chem. A*, 2014, **2**, 4384–4390.
246 S. Su, C. Zhang, L. Yuwen, X. Liu, L. Wang, C. Fan and L. Wang, *Nanoscale*, 2016, **8**, 602–608.
247 J. Bai, X. Xiao, Y. Y. Xue, J. X. Jiang, J. H. Zeng, X. F. Li and Y. Chen, *ACS Appl. Mater. Interfaces*, 2018, **10**, 19755–19763.
248 H. Xu, P. Song, J. Wang, F. Gao, Y. Zhang, Y. Shiraishi and Y. Du, *ChemCatChem*, 2018, **10**, 2195–2199.
249 F. Wang, K. Wang, C. An, C. An and W. Zhang, *J. Colloid Interface Sci.*, 2020, **571**, 118–125.
250 K. Zhang, D. Bin, B. Yang, C. Wang, F. Ren and Y. Du, *Nanoscale*, 2015, **7**, 12445–12451.
251 Y. Liang, Q. Wu and F. Liang, *Chin. J. Anal. Chem.*, 2021, **49**, 21087–21095.
252 S. Shen and T. Zhao, *J. Mater. Chem. A*, 2013, **1**, 906–912.
253 B. Lan, M. Huang, R. L. Wei, C. N. Wang, Q. L. Wang and Y. Y. Yang, *Small*, 2020, **16**, e2004380.
254 S. Bai, Y. Xu, K. Cao and X. Huang, *Adv. Mater.*, 2021, **33**, e2005767.
255 L. Xiao, G. Li, Z. Yang, K. Chen, R. Zhou, H. Liao, Q. Xu and J. Xu, *Adv. Funct. Mater.*, 2021, **31**, 2100982.
256 Q. Chang, Y. Hong, H. J. Lee, J. H. Lee, D. Ologunagba, Z. Liang, J. Kim, M. J. Kim, J. W. Hong, L. Song, S. Kattel, Z. Chen, J. G. Chen and S. I. Choi, *Proc. Natl. Acad. Sci. U. S. A.*, 2022, **119**, e2112109119.
257 D. Kim, Y. W. Lee, S. B. Lee and S. W. Han, *Angew. Chem., Int. Ed.*, 2012, **51**, 159–163.
258 Y. Kang, L. Qi, M. Li, R. E. Diaz, D. Su, R. R. Adzic, E. Stach, J. Li and C. B. Murray, *ACS Nano*, 2012, **6**, 2818–2825.
259 X. H. Xia and T. Iwasita, *J. Electrochem. Soc.*, 1993, **140**, 2559–2565.
260 J. Wang, D. F. Thomas and A. Chen, *Chem. Commun.*, 2008, 5010–5012.
261 X. Qu, Z. Cao, B. Zhang, X. Tian, F. Zhu, Z. Zhang, Y. Jiang and S. Sun, *Chem. Commun.*, 2016, **52**, 4493–4496.
262 M. Wu, C. Zhu, K. Wang, G. Li, X. Dong, Y. Song, J. Xue, W. Chen, W. Wei and Y. Sun, *ACS Appl. Mater. Interfaces*, 2020, **12**, 11562–11569.
263 R. Zhou, X. Fan, X. Ke, J. Xu, X. Zhao, L. Jia, B. Pan, N. Han, L. Li, X. Liu, J. Luo, H. Lin and Y. Li, *Nano Lett.*, 2021, **21**, 4092–4098.
264 H. Xie, Y. Wan, X. Wang, J. Liang, G. Lu, T. Wang, G. Chai, N. M. Adli, C. Priest, Y. Huang, G. Wu and Q. Li, *Appl. Catal., B*, 2021, **289**, 119783.
265 M. Yang, R. Alvarez-Puebla, H. S. Kim, P. Aldeanueva-Potel, L. M. Liz-Marzan and N. A. Kotov, *Nano Lett.*, 2010, **10**, 4013–4019.
266 L. Rodríguez-Lorenzo, R. A. Álvarez-Puebla, F. J. G. D. Abajo and L. M. Liz-Marzán, *J. Phys. Chem. C*, 2010, **114**, 7336–7340.
267 C. G. Khoury and T. Vo-Dinh, *J. Phys. Chem. C*, 2008, **112**, 18849–18859.
268 M. Ceballos, A. Arizmendi-Morquecho, M. Sánchez-Domínguez and I. López, *Mater. Chem. Phys.*, 2020, **240**, 122225.
269 S. Wang, L. P. Xu, Y. Wen, H. Du, S. Wang and X. Zhang, *Nanoscale*, 2013, **5**, 4284–4290.
270 L. F. Zhang, S. L. Zhong and A. W. Xu, *Angew. Chem., Int. Ed.*, 2013, **52**, 645–659.
271 H. B. Li, P. Liu, Y. Liang, J. Xiao and G. W. Yang, *Nanoscale*, 2012, **4**, 5082–5091.
272 W. Jia, J. Li and L. Jiang, *ACS Appl. Mater. Interfaces*, 2013, **5**, 6886–6892.
273 A. G. da Silva, M. L. de Souza, T. S. Rodrigues, R. S. Alves, M. L. Temperini and P. H. Camargo, *Chem. – Eur. J.*, 2014, **20**, 15040–15046.
274 Y. Xia and J. Wang, *Mater. Chem. Phys.*, 2011, **125**, 267–270.
275 P. Kannan, J. Dolinska, T. Maiyalagan and M. Opallo, *Nanoscale*, 2014, **6**, 11169–11176.
276 L. D. Rafailović, C. Gammer, J. Srajer, T. Trišović, J. Rahel and H. P. Karnthaler, *RSC Adv.*, 2016, **6**, 33348–33352.
277 L. Soleymani, Z. Fang, E. H. Sargent and S. O. Kelley, *Nat. Nanotechnol.*, 2009, **4**, 844–848.
278 S. O. Kelley, C. A. Mirkin, D. R. Walt, R. F. Ismagilov, M. Toner and E. H. Sargent, *Nat. Nanotechnol.*, 2014, **9**, 969–980.
279 Y. Song, T. Xu, Q. Zhu and X. Zhang, *Biosens. Bioelectron.*, 2020, **162**, 112253.
280 Y. Song, T. Xu, L. P. Xu and X. Zhang, *Nanoscale*, 2018, **10**, 20990–20994.
281 T. Xu, Y. Song, W. Gao, T. Wu, L. P. Xu, X. Zhang and S. Wang, *ACS Sens.*, 2018, **3**, 72–78.
282 X. He, S. Yang, T. Xu, Y. Song and X. Zhang, *Biosens. Bioelectron.*, 2020, **152**, 112013.
283 A. O. Oladipo, T. T. I. Nkambule, B. B. Mamba and T. A. M. Msagati, *Nanoscale Adv.*, 2020, **2**, 5152–5165.
284 X. Liu, X. Zhang, M. Zhu, G. Lin, J. Liu, Z. Zhou, X. Tian and Y. Pan, *ACS Appl. Mater. Interfaces*, 2017, **9**, 279–285.
285 P. Qiu, M. Yang, X. Qu, Y. Huai, Y. Zhu and C. Mao, *Biomaterials*, 2016, **104**, 138–144.
286 J. H. Byeon and Y. W. Kim, *ACS Macro Lett.*, 2014, **3**, 205–210.
287 Y. Deng, X. Tian, S. Lu, M. Xie, H. Hu, R. Zhang, F. Lv, L. Cheng, H. Gu, Y. Zhao and Y. Pan, *ACS Appl. Mater. Interfaces*, 2018, **10**, 31106–31113.
288 A. O. Oladipo, T. T. I. Nkambule, B. B. Mamba and T. A. M. Msagati, *Mater. Sci. Eng., C*, 2020, **110**, 110696.
289 J. Bai, L. Shen, D. Sun, Y. Tang and T. Lu, *CrystEngComm*, 2014, **16**, 10445–10450.
290 C. B. Whitehead and R. G. Finke, *Mater. Adv.*, 2021, **2**, 6532–6568.
291 K. Guo, D. Fan, J. Bao, Y. Li and D. Xu, *Adv. Funct. Mater.*, 2022, 2208057.